Author Manuscript

Surface and sub-surface kinetic energy wavenumber-frequency spectra in global ocean models and observations

Joseph K. Ansong,[1,2*], Brian K. Arbic[1], Arin D. Nelson[1,3], Matthew H. Alford[4], Eric Kunze[5], Dimitris Menemenlis[6], Anna C. Savage[1,7], Jay F. Shriver[8], Alan J. Wallcraft[9], Maarten C. Buijsman[10]

[1]Department of Earth & Environmental Sciences, University of Michigan, Ann Arbor, Michigan, USA.
[2]Department of Mathematics, University of Ghana, Accra, Ghana.
[3]Naval Undersea Warfare Center, Newport, Rhode Island, USA.
[4]Scripps Institution of Oceanography, University of California, San Diego, USA.
[5]NorthWest Research Associates, Redmond, Washington, USA.
[6]Earth Sciences Division, Jet Propulsion Laboratory, California Institute of Technology, Pasadena, CA, USA.
[7]Running Tide, Portland, Maine, USA.
[8]Ocean Dynamics and Prediction Branch, Code 7323, Naval Research Laboratory, Stennis Space Center, MS, USA.
[9]Center for Ocean and Atmospheric Prediction, Florida State University, Tallahassee, FL, USA.
[10]Department of Marine Science, University of Southern Mississippi, 1020 Balch Blvd, Stennis Space Center, MS, USA.

Key Points:

- Wavenumber-frequency spectra of kinetic energy are computed from two high-resolution global models and compared with observations.
- Both models under-estimate motions at high vertical wavenumbers (small vertical scales), flagging this as a target for model improvement.
- The ratio of high- vs low-frequency surface kinetic energy at small horizontal scales is dependent on the model and grid spacings employed.

*Current address: Department of Mathematics, University of Ghana, Legon, Accra

Corresponding author: Joseph K. Ansong, jkansong@ug.edu.gh

This is the author manuscript accepted for publication and has undergone full peer review but has not been through the copyediting, typesetting, pagination and proofreading process, which may lead to differences between this version and the Version of Record. Please cite this article as doi: 10.1029/2023JC020480.

This article is protected by copyright. All rights reserved.

Author Manuscript

Abstract

This paper examines spectra of horizontal kinetic energy (HKE) in the surface and sub-surface ocean, with an emphasis on internal gravity wave (IGW) motions, in global high-resolution ocean simulations. Horizontal wavenumber-frequency spectra of surface HKE are computed over seven oceanic regions from two global simulations of the HYbrid Coordinate Ocean Model (HYCOM) and three global simulations of the Massachusetts Institute of Technology general circulation model (MITgcm). In regions with high IGW activity, high surface HKE variance in the horizontal wavenumber-frequency spectra is aligned along IGW linear dispersion curves. For both HYCOM and MITgcm, and in almost all regions, finer horizontal resolution yields more energetic supertidal IGW continuum spectra. The ratio of high-horizontal-wavenumber variance in semi-diurnal and supertidal motions relative to lower-frequency motions, a quantity of great interest for swath altimetry, depends on the model employed and the horizontal resolution within the model, implying that quantitative predictions of the partition between low- and high-frequency motions taken from particular simulations should be treated with care. The frequency-vertical wavenumber spectra, frequency spectra, and vertical wavenumber spectra from the models are compared to spectra computed from McLane profilers at nine locations. In general, MITgcm spectra match the McLane profiler spectra more closely at high frequencies ($|\omega| > 4.5\,\mathrm{cpd}$). In both models, vertical wavenumber spectra roll off more steeply than observations at high vertical wavenumbers ($m > 10^{-2}\,\mathrm{cpm}$). The vertical wavenumber spectra in such models is an important target for improvement, due to turbulence production and dissipation that takes place at high vertical wavenumbers.

Plain Language Summary

Recently, a small but growing number of global ocean models have begun to employ simultaneous tidal and atmospheric forcing. At the same time, increasing supercomputer power has allowed for simulations of oceanic motions with increasing accuracy, increasing feature (spatial) resolution, and more frequent time slices. Global ocean models with fine grid spacing, and simultaneous tidal and atmospheric forcing, host a vigorous spectrum of high-frequency waves that control mixing over most of the ocean water column, and are important for many operational oceanography challenges. As an example of the latter, high-resolution global internal wave models have been used to study the relative partition of high-frequency vs. low-frequency motions at the small horizontal scales that will be measured by the new Surface Water Ocean Topography (SWOT) mission. The partition described above depends on the model employed and the grid spacing employed within that model, meaning that conclusions about the partition are dependent on the model used to estimate it. Comparisons between the models and vertically profiling instruments indicate that resolving fine scale motions in the vertical direction, where ocean mixing takes place, is not yet handled well by the models. Modeling of fine-vertical scale motions is therefore an important future research direction.

1 Introduction

This paper examines the relative amounts of energy in low-frequency eddy motions vs. high-frequency internal gravity wave (IGW) motions at high horizontal wavenumbers (small horizontal scales) in horizontal wavenumber spectra of sea surface height (SSH) in global IGW models, and the sensitivity of the model predictions of this partition to grid spacing and commonly used parameterizations. We also examine the comparison of vertical wavenumber spectra in global IGW models to in-situ observations. The partition of high-frequency IGW and low-frequency eddy energy at small horizontal scales is of utmost importance for the new Surface Water Ocean Topography (SWOT) mission, which is measuring SSH at finer resolution than previous nadir (downward-looking) missions (Morrow et al., 2019). Furthermore, SWOT measures SSH in two-dimensional swaths

This article is protected by copyright. All rights reserved.

Author Manuscript

rather than the one-dimensional tracks of nadir missions. As with nadir altimetry, SWOT altimetry will be used to estimate geostrophic motions; but that requires separation of geostrophic vs. wave motions in the SSH field (Richman et al., 2012; Rocha et al., 2016a; Savage, Arbic, Alford, et al., 2017; Torres et al., 2018). The global IGW models used here have been used to anticipate SWOT measurements (J. Wang et al., 2018) and will now be used to interpret them. It is therefore important to assess the realism of global IGW models. In past papers we and other authors have assessed this realism through comparisons with nadir altimetry (Shriver et al., 2012; Ansong et al., 2015; Buijsman et al., 2020) and in-situ measurements from current meters, drifters, and other instruments (M. Müller et al., 2015; Rocha et al., 2016a; Ansong et al., 2017; Luecke et al., 2020; Yu et al., 2019; Arbic et al., 2022). Here, for the first time, we compute vertical wavenumber spectra from global IGW models, and compare the model spectra to spectra computed from in-situ vertical profiling instruments. The vertical wavenumber spectra reveal an important limitation of the models, that we are already striving to rectify using results from regional models. Both our horizontal wavenumber and vertical wavenumber spectra are also computed as a function of frequency, in order to separate low-frequency eddying motions from high-frequency IGW motions.

Internal gravity waves (IGWs), argued by Munk and Wunsch (1998) and others to be the main drivers of vertical mixing in the stratified open ocean (e.g., Kunze, 2017b, 2017a; de Lavergne et al., 2016), play an important role in ocean dynamics by transporting energy throughout the water column and over $\sim O(1000\,\mathrm{km})$ distances. Recent advances in understanding internal wave-driven mixing in the ocean interior have been summarized in MacKinnon et al. (2017). IGWs have wide-ranging space and time scales. The Garrett-Munk (GM) spectrum (Garrett & Munk, 1972, 1975; Cairns & Williams, 1976) generally provides a useful statistical description of the high-frequency (supertidal) open-ocean IGW continuum (Levine, 2002; Wunsch & Ferrari, 2004). Traditionally, the two major energy sources of oceanic IGWs are thought to be surface winds and astronomical tidal forcing(Olbers, 1976; C. McComas, 1977; C. H. McComas & Bretherton, 1977; C. H. McComas & Müller, 1981b, 1981a; P. Müller et al., 1986; Polzin, 2004). Wind forcing generates near-inertial waves which propagate into the ocean interior (e.g., Simmons & Alford, 2012; Raja et al., 2022). Barotropic tidal flow over rough topography generates internal tides (internal gravity waves at tidal frequency). High-vertical mode internal tides dissipate near their generation sources while low-vertical mode internal tides propagate over long distances (e.g., Dushaw et al., 1995; Ray & Mitchum, 1996; Mitchum & Chiswell, 2000; Simmons et al., 2004; Zhao et al., 2010). While the near-inertial motions and internal tides occupy discrete and narrow ranges in spectral space, it has been argued that nonlinear interactions between them produce the broadband IGW spectrum (e.g., P. Müller et al., 1986; Sugiyama et al., 2009; Skitka et al., 2024). See Barkan et al. (2017), Delpech et al. (2024) and others for discussions of the potential role of mesoscale eddies in catalyzing the IGW continuum spectrum.

Internal gravity waves can be measured using in-situ instruments and satellites. However, because in-situ measurements are geographically sparse and satellite measurements suffer from infrequent temporal sampling, neither cover the global space-time variability of the IGW field. Global IGW models are relatively well-sampled in space and time and can help to better understand their amplitudes and space-time scales in different oceanic regions. To simulate IGWs globally, models should simultaneously include (a) atmospheric forcing, updated frequently, in order to simulate near-inertial waves, (b) astronomical tidal forcing, to obtain the barotropic tides and hence the internal tides, and (c) horizontal and vertical grid spacings that are fine enough to produce vigorous nonlinear interactions. Several centers around the world have recently begun to run models that meet these criteria (Arbic et al., 2010, 2012; Buijsman et al., 2020; M. Müller et al., 2012; Rocha et al., 2016a, 2016b); see Arbic et al. (2018) and Arbic (2022) for reviews of global internal wave models. M. Müller et al. (2015) showed that present-day high-resolution global models that are simultaneously forced by atmospheric fields and tides are able to sim-

This article is protected by copyright. All rights reserved.

Author Manuscript

ulate part of the IGW spectrum. M. Müller et al. (2015) focused on the frequency and frequency-horizontal wavenumber spectra of surface horizontal kinetic energy (HKE) in the HYbrid Coordinate Ocean Model (HYCOM; Bleck, 2002; Chassignet et al., 2009; Halliwell, 2004), and showed that modeled spectra follow the predicted IGW dispersion curves. Müller et al. also compared surface HKE frequency spectra in models and current-meter observations. Subsequent analyses (Rocha et al., 2016a, 2016b; Qiu et al., 2018; Torres et al., 2018; J. Wang et al., 2019) of global internal wave simulations of the Massachusetts Institute of Technology general circulation model (MITgcm; Marshall et al., 1997) demonstrated similar surface HKE spectral concentration along predicted IGW dispersion curves. Comparison of spectra from global HYCOM and MITgcm internal wave simulations with each other and with observations from moored current meters (Savage, Arbic, Alford, et al., 2017; Luecke et al., 2020) demonstrated that supertidal spectra from MITgcm simulations with 1/48° grid spacing are more energetic and lie closer to observations than spectra from HYCOM simulations with 1/25° grid spacing. This paper will examine the sensitivities of the modeled IGWs to the grid spacings employed in the simulations, in both HYCOM and MITgcm.

Many analyses of internal tide and IGW continuum horizontal wavenumber spectra in global models (Richman et al., 2012; Savage, Arbic, Alford, et al., 2017; Qiu et al., 2018; Torres et al., 2018; J. Wang et al., 2019) have focused on IGW surface HKE and SSH signals. This focus on the surface is motivated by interest in the partition of high-frequency IGW vs. low-frequency eddy motions in observations of the SWOT mission (Fu et al., 2012; Morrow et al., 2019), which has begun to measure SSH in fine-scale, two-dimensional swaths rather than the coarser-scale one-dimensional tracks of traditional nadir altimeter missions. In regions with strong IGWs, IGW motions may obscure the measurement of low-frequency eddying motions, especially because the relatively infrequent temporal sampling of SWOT may not allow separation of IGWs and eddy motions in the time-domain. Motivated by consideration of SWOT, Qiu et al. (2018) employed a dynamically defined transition length scale for separating low-frequency eddy and high-frequency internal wave motions. As in several other studies of the 1/48° MITgcm simulations, Qiu et al. (2018) did not compare different results from different resolutions of the same model (MITgcm), or compare results from different models (MITgcm vs. HYCOM). Here, we will examine the partition between low-frequency and high-frequency surface HKE as a function of the model used and the resolution employed, to determine whether quantitative conclusions about this partition drawn from any particular simulation are sensitive to details of that simulation. We will analyze global simulations from seven oceanic regions chosen to represent areas with different oceanic dynamics, and will analyze two separate high-resolution global models, HYCOM and MITgcm, both forced by atmospheric fields and tides. As in Savage, Arbic, Alford, et al. (2017) and Luecke et al. (2020), we examine HYCOM simulations with two different grid spacings (1/12° and 1/24°) and MITgcm simulations with three different grid spacings (1/12°, 1/24° and 1/48°).

This paper also examines the sub-surface HKE field, through computations of vertical wavenumber and vertical wavenumber-frequency spectra. Vertical wavenumber spectra are important because they inform us about the extent to which the modeled fields of IGW and other motions are reaching small vertical length scales, where overturning and mixing takes place. There is a vast literature on vertical wavenumber spectra written by the IGW observational community (e.g., Gargett et al., 1981; Gregg et al., 1993; Leaman, 1976; Alford et al., 2017). Thus, computing vertical wavenumber spectra from global models connects more naturally to the historical IGW literature than computing horizontal wavenumber spectra. Here we will compute vertical wavenumber and vertical wavenumber-frequency spectra from the five HYCOM and MITgcm simulations described above, and compare the results to moored McLane Profilers (MMPs; Doherty et al., 1999; Alford et al., 2007). To our knowledge, our study is the first to compare vertical wavenumber and vertical wavenumber-frequency spectra in global models to obser-

This article is protected by copyright. All rights reserved.

Author Manuscript

vations. We have recently compared frequency-, frequency-vertical wavenumber, and vertical wavenumber spectra in regional simulations of MITgcm to observations (Nelson et al., 2020; Thakur et al., 2022). Nelson et al. (2020) demonstrate that frequency spectra in regional MITgcm simulations run with horizontal and vertical grid spacings much finer than is feasible in global simulations lie closer to observations than do frequency spectra in global simulations, which fall off steeply at very high frequencies ($\gtrsim 6$ cpd). Rather than focusing on very high-resolution regional simulations, Thakur et al. (2022) instead examine the impact of the background KPP (Large et al., 1994) parameterization in MITgcm simulations run at approximately similar resolutions as in global models. Thakur et al. (2022) found that turning off the background KPP setting, which is meant to account for IGW activity that is absent from most ocean models, yielded vertical wavenumber spectra in MITgcm runs that rolled off less steeply and compared more closely to observations than spectra in simulations with the background KPP on. Thakur et al. (2022) showed that turning off background KPP values affected the vertical wavenumber spectra across a wide range of frequencies; thus, the vertical wavenumber spectra results are applicable to more than just IGW motions. Currently available global simulations of MITgcm and HYCOM employ nonzero background KPP values. Based upon the results of Thakur et al. (2022), we anticipate that these nonzero background KPP values in currently available global HYCOM and MITgcm simulations will impact the vertical wavenumber spectra of modeled oceanic motions; we will examine that hypothesis here. We note that vertical wavenumber and horizontal wavenumber spectra are not independent of each other. For instance, IGW vertical wavenumbers, horizontal wavenumbers and frequencies are connected to each other via the internal wave dispersion relation. Thus our examination of vertical wavenumber spectra may have implications for the horizontal wavenumber spectra of SSH, the quantity of central interest for SWOT.

2 The model simulations and observations

The next three subsections briefly describe the numerical simulations and observational data used in this study. We compute horizontal wavenumber-frequency spectra of surface HKE from the same seven regions examined in Savage, Arbic, Alford, et al. (2017), who computed horizontal wavenumber-frequency spectra of SSH from the same MITgcm and HYCOM simulations. The seven regions examined are shown in Figure 1 and described in Table 1. The minimum and maximum depths in each region are listed in Table 1. The model output is relatively short (~ 90 days) and is not always taken from the same season for different simulations. This reflects what was available to us at the time we began these analyses in 2015; the computational limits on running and analyzing model outputs of this size are still considerable, and were even more so in 2015. (Although we began our analyses in 2015, it is still the case that the resolutions of our HYCOM and MITgcm simulations are state-of-the-art today). The Moored McLane Profiler data records are also short, typically of order 30 days, and are taken from different seasons at different locations. Such sampling problems are typical of model-data comparisons; see discussions in Luecke et al. (2020) and Arbic et al. (2022). Another limitation of the study is that the vertical grid spacings were set up with many considerations, especially computational feasibility, in mind, and are not optimally set up for resolving vertical baroclinic modes of IGWs and other oceanic motions.

As expounded upon in subsection 2.3, time-series from nine McLane profilers are compared to the nearest model grid points. Thus, as far as the models' horizontal resolution allows, there is no spatial mismatch between model and profiler locations, but we expect grid points from 1/48° MITgcm simulation to be generally closer to profiler locations because of its higher horizontal resolution. Both MITgcm and HYCOM were run in hydrostatic configurations.

This article is protected by copyright. All rights reserved.

Author Manuscript

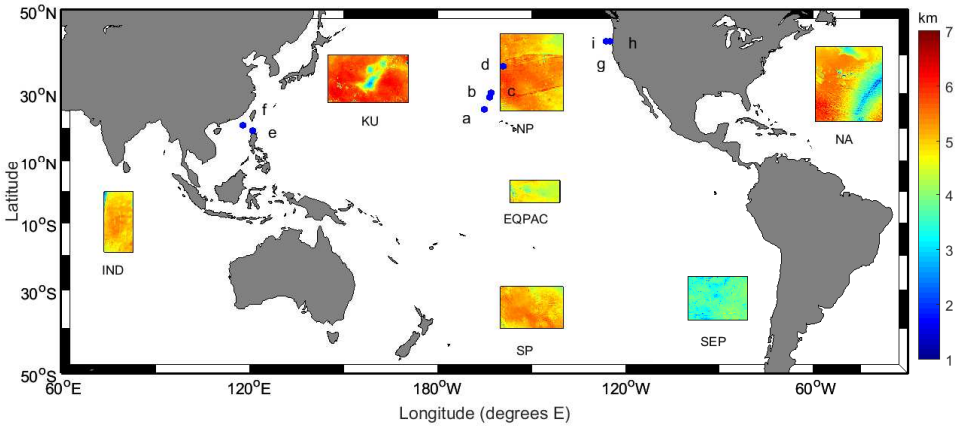


Figure 1. Bathymetries (in km; from MITgcm48) for the seven regions in this study. "MITgcm48" is shorthand for 1/48° MITgcm simulation. Key: KU=Kuroshio, NP=North Pacific, NA= North Atlantic, EQPAC= Equatorial Pacific, SP=South Pacific, SEP= South East Pacific, IND=Indian Ocean. More details are in Table 1. Blue dots indicate the locations of nine North Pacific McLane profilers used in this study (Table 3).

This article is protected by copyright. All rights reserved.

Author Manuscript

Table 1. The names, locations and depth ranges of the seven regions used in this study.

Region		Location		Depth (m)	
Full Name	Abbreviation	Latitudes	Longitudes	Min.	Max.
North Pacific	NP	25.00– 44.99°	200.01– 219.99°E	988.60	6680.10
North Atlantic	NA	22.00– 42.00°	300.61– 321.99°E	805.31	7000.04
Kuroshio	KU	27.36– 39.99°	145.01– 170.61°E	900.49	7000.04
South East Pacific	SEP	-37.99– -26.23°	260.01– 279.09°E	1165.77	5081.51
South Pacific	SP	-39.99– -29.01°	200.01– 219.99°E	1009.98	6520.30
Equatorial Pacific	EQPAC	-3.49° – 3.49°	202.97– 218.99°E	1136.45	5553.29
Indian Ocean	IND	-18.99– -0.01°	73.61 – 82.99°E	959.57	6021.93

2.1 The HYCOM simulations

This study employs free-running (non-data-assimilative) HYCOM simulations run at high vertical and horizontal resolutions by the United States Navy, which runs data-assimilative HYCOM simulations for operational purposes (Metzger et al., 2014). The simulations used here have 41 hybrid vertical coordinate surfaces. The hybrid simulations employ z (depth) coordinates in the open-ocean mixed layer, density coordinates in the open-ocean beneath the mixed layer, and terrain-following coordinates in shallow coastal regions. The nominal horizontal resolutions at the equator of the simulations examined here are 1/12.5° (HYCOM12) and 1/25° (HYCOM25). The simulations are forced by the five largest semidiurnal and diurnal tidal constituents (M_2, S_2, N_2, K_1, O_1) as well as by atmospheric pressure, wind and buoyancy forcing from the Navy Global Environmental Model (NAVGEM; Hogan et al., 2014). Atmospheric forcing is applied at hourly intervals in HYCOM12 and 3-hourly intervals in HYCOM25. Both simulations employ tidal self-attraction and loading (SAL; Hendershott, 1972; Ray, 1998) fields taken from the data-assimilative TPXO8-atlas (Egbert & Erofeeva, 2002) and use the parameterized topographic wave drag scheme of Jayne and St Laurent (2001). Previous studies based upon HYCOM demonstrate the importance of parameterized topographic wave drag, which accounts for unresolved IGW breaking processes, for bringing barotropic and low-mode baroclinic tidal amplitudes close to observations (Shriver et al., 2012; Ansong et al., 2015; Buijsman et al., 2016, 2020). The simulations utilized here incorporate an Augmented State Ensemble Kalman filter (ASEnKF; Ngodock et al., 2016) to reduce barotropic tidal SSH errors. The M_2 sea surface elevation error equatorward of 66° for seafloor depths exceeding 1000 m is 2.6 cm (Ngodock et al., 2016). This error is substantially lower than errors reported in most published studies of purely forward tide models, but is not yet at the levels seen in the very best data-assimilative barotropic tide models (e.g., Stammer et al., 2014). The 1/12.5° simulation was run from July 2011 through October 2012 and the 1/25° simulation from November 2013 through December 2014 (Table 2). Unfortunately, the HYCOM simulations suffer from a numerical instability in the high-latitude North Pacific (south of the Aleutians). This instability can be seen, for example, in our analyses in Buijsman et al. (2016) and Arbic et al. (2022). HYCOM results in the North Pacific region of this paper will be affected by this instability. However, HYCOM results in other regions are unaffected.

2.2 The MITgcm simulations

This study uses three MITgcm simulations with 90 vertical levels. The level thicknesses range from 1.0 m at the surface to 480 m near the bottom at a maximum model depth of 7 km. The simulations were run at horizontal resolutions of 1/12° (3 − 9 km grid spacing; referred to as MITgcm12), 1/24° (2−5 km grid spacing; referred to as MITgcm24), and 1/48° (0.75−2.3 km grid spacing; referred to as MITgcm48). Surface forc-

This article is protected by copyright. All rights reserved.

Author Manuscript

Table 2. Names, nominal model horizontal resolution, and record times of the five simulations used in this study.

Abbreviation	Horizontal resolution	Record times
HYCOM12	1/12.5°	October 27, 2011– January 24, 2012
HYCOM25	1/25°	January 1, 2014– March 31, 2014
MITgcm12	1/12°	March 1, 2014– May 29, 2014
MITgcm24	1/24°	October 31, 2011– January 28, 2012
MITgcm48	1/48°	October 31, 2011– January 28, 2012

ing of the model uses six-hourly atmospheric fields from the 0.14° European Center for Medium-Range Weather Forecasts (ECMWF) atmospheric operational model analysis. The sea ice model of Losch et al. (2010) is used to compute ocean surface fluxes over ice-covered regions. MITgcm forcing differs from HYCOM. Tidal forcing is from the full lunisolar potential (not 16 constituents, as claimed by Savage, Arbic, Alford, et al. (2017)) and is applied to MITgcm as an additional atmospheric pressure forcing (Ponte et al., 2015). Forcing with a tidal potential is equivalent to having atmospheric pressure loading, as discussed in detail by Ponte and Vinogradov (2007). In contrast to the HYCOM simulations, the MITgcm simulations do not employ a parameterized topographic wave drag. The MITgcm12 simulation is initialized on 1 January 2010 from a data-constrained 1/6° simulation provided by the "Estimating the Circulation and Climate of the Ocean, Phase II (ECCO2)" project (Menemenlis et al., 2008) and integrated for one year without tides with ERA-Interim (Dee et al., 2011) surface boundary conditions. The MITgcm24 simulation is initialized from MITgcm12 fields on 17 January 2011. Starting in 2011, ECMWF is converted to surface fluxes using the bulk formulae of Large and Yeager (2004). Thus, the model simulation uses the Large and Yeager (2004) bulk formulae and the dynamic/thermodynamic sea ice model of Losch et al. (2010) to convert ECMWF atmospheric conditions to ocean surface fluxes. The ocean surface stress accounts for the velocity of wind and ocean currents as discussed in Flexas et al. (2019). Additional descriptions of the MITgcm24 and MITgcm48 simulations may be found in Rocha et al. (2016a, 2016b), Arbic et al. (2018), Arbic (2022), and Arbic et al. (2022). Here, we employ 90 days of hourly model output from the three simulations for the periods: 1 March 2014 through 29 May 2014 for MITgcm12 and 31 October 2011 through 28 January 2012 for MITgcm24 and MITgcm48 (see Table 2).

Comparisons to global surface and near-surface drifter datasets (Elipot et al., 2016) provide a useful viewpoint on the realism of high- (and low-) frequency kinetic energy in these simulations. The six-hourly atmospheric forcing of the MITgcm simulations yields near-inertial flows that are insufficiently energetic with respect to drifter observations (Yu et al., 2019; Arbic et al., 2022). In contrast, HYCOM near-inertial flows lie closer to drifter observations due to more frequently updated atmospheric forcing (Arbic et al., 2022). Semidiurnal tidal kinetic energy is substantially higher in MITgcm simulations than in drifter observations (Yu et al., 2019; Arbic et al., 2022), due to the lack of parameterized topographic wave drag in MITgcm, whereas semidiurnal kinetic energy in HYCOM lies closer to drifter values (Arbic et al., 2022).

Some initial computations of the vertical wavenumber-frequency spectra in global MITgcm48 output were performed in Wunsch (2016) (unpublished manuscript). Our earlier calculations of vertical wavenumber-frequency spectra followed that in Wunsch (2016), but our final results employ rotary frequency-vertical wavenumber spectra following Alford et al. (2017).

This article is protected by copyright. All rights reserved.

Author Manuscript

2.3 The McLane profiler data

Time-series from nine McLane profilers (Doherty et al., 1999) are compared to the nearest model grid points (Figure 1, Table 3). All the profilers are in the North Pacific with *a*-*d* around Hawai'i (Alford et al., 2007; Zhao et al., 2010; MacKinnon et al., 2013b, 2013a), *e*-*f* in Luzon Strait (Alford et al., 2011) and *g*-*i* off the coast of Oregon (Nash et al., 2007; Martini et al., 2011, 2013). The vertically sampled velocity, temperature and salinity are mapped onto 2 db vertical intervals. Only profilers in locations with seafloor depths greater than 1 km are used. Record durations are 22-51 days. Sampling periods are approximately one hour but vary between locations. Frequency spectra of steric SSH computed from these profilers were compared to spectra of SSH computed from the same five simulations examined here in Savage, Arbic, Alford, et al. (2017). Here we will perform a model-profiler comparison with a focus on frequency-vertical wavenumber spectra of HKE. The models are not co-located in time with the observations, but Kunze (2017b), who infers diapycnal diffusivities and IGW strain from repeat hydrography sections (their Figs. 4 and 6), demonstrates repeatability of IGW signals over many years.

Table 3. The McLane moored profilers used in this study.

Mooring		Location		Pressure		Date & Length	
Profiler ID	Name	Lat.	Lon.	Min.	Max.	Start Date	Record Length (Days)
a	IWAP MP1	25.5°N	194.8°E	97	1403	Apr 25, 2006	36
b	IWAP MP3	28.9°N	196.5°E	97	1418	May 10, 2006	34
c	IWAP MP4	30.1°N	197.1°E	97	1430	Apr 25, 2006	22
d	IWAP MP6	37.1°N	200.8°E	97	1410	Apr 25, 2006	22
e	IWISE H04	19.3°N	121.0°E	373	1223	June 17, 2011	51
f	SCS MP1	20.9°N	117.9°E	111	1303	May 6, 2007	31
g	ORE MP1	43.2°N	233.7°E	138	2121	Sept 15, 2005	40
h	ORE MP4	43.9°N	234.9°E	73	1332	Sept 14, 2005	40
i	ORE MP5	43.2°N	235.0°E	236	1063	Sept 13, 2005	40

3 Methods

3.1 Rotary Spectra & WKB-scaling

This section describes the methodology employed to compare nine McLane profiler time series of HKE with those from the nearest model grid points in HYCOM25 and MITgcm48. Horizontal velocities were combined into a single complex velocity variable

$$\tilde{u}(z,t) = u(z,t) + iv(z,t),$$

where z and t are vertical position and time respectively. Data above the deepest observed mixed-layer depth, taken to be 200 db, was ignored.

Internal waves propagating vertically through the ocean's depth- and time-varying stratification experience refraction, which affects their amplitude and vertical wavenumber. To account for this, subsurface ocean velocity measurements are typically WKB-scaled to the same time-mean stratification at all depths and observation locations. This allows for meaningful comparisons between regions with different stratifications (Leaman, 1976). Here, WKB scaling is performed utilizing the variable η:

$$\eta^2(z) = \overline{N^2(z,t)}/N_0^2,$$

This article is protected by copyright. All rights reserved.

Author Manuscript

where $\overline{N^2(z,t)}$ is the time-mean of the square of the buoyancy frequency N, computed via the Thermodynamic Equation of Seawater 2010 (TEOS-10; Wright et al., 2011) using a reference pressure of 1 db. N_0 is a constant reference value taken as $0.0042\,\mathrm{s}^{-1}$ (e.g., Alford et al., 2017). The time mean of N^2 is used instead of the time mean of N because N^2 is the quantity that is present in the vertical momentum equation of ocean fluid motion. WKB-scaled horizontal velocity $\tilde{u}'$ can be computed via

$$\tilde{u}(z,t)' = \tilde{u}(z,t)/\sqrt{\eta(z)}.$$

Depth is WKB-stretched as

$$z' = \int_{200}^{z} \eta(\hat{z}) d\hat{z}.$$

WKB-scaled rotary velocities were interpolated onto evenly-spaced WKB-stretched depth levels from 200 to 1000 db with 2 db spacing. Analyses were limited to depths shallower than 1000 db due to instrument noise below this depth. This limitation and the 200-m depth upper bound mean that the analysis is confined to the main pycnocline.

Frequency and vertical wavenumber spectral densities of WKB-scaled horizontal velocity were computed using a discrete two-dimensional Fourier transform. The all-time means were removed at each depth, and a Tukey window with a taper-to-constant ratio of 0.2 was applied in both depth and time. From this rotary spectra, the depth-averaged frequency spectral densities were computed by integrating the rotary spectrum across all vertical wavenumbers at each frequency. A similar procedure was performed to compute the time-averaged vertical wavenumber spectral densities. Rotary-with-depth analyses are also employed to separate the complex velocity signal into clockwise (CW) and counter-clockwise (CCW) components and identify up- and downgoing energy as explained in section 4. Groundbreaking papers about rotary-with-depth analyses include Leaman and Sanford (1975); Kunze and Sanford (1984); D'Asaro and Perkins (1984); Pinkel (1985); Waterhouse et al. (2022). Kunze and Sanford (1984) include the formulae in their paper.

3.2 Frequency-Horizontal Wavenumber Spectral Density

Frequency-horizontal wavenumber spectral densities of surface HKE are computed using 90 days of hourly time series (see Table 2) with discrete two-dimensional Fourier transforms. Additional details of this procedure are given in Savage, Arbic, Alford, et al. (2017). Temporal and two-dimensional spatial trends are first removed and a Tukey window with a taper-to-constant ratio of 0.2 was applied before computing the spectral densities.

As in M. Müller et al. (2015) and Savage, Arbic, Alford, et al. (2017), we compute the internal gravity wave linear dispersion relation curves by solving for eigenspeeds using the Sturm-Liouville equation for vertical modes (e.g., Munk, 1981; Ansong et al., 2017; Arbic et al., 2018, amongst many references). The Sturm-Liouville problem assumes a constant seafloor depth H, Coriolis frequency f and buoyancy frequency N_0. We use extreme eigenspeed values, as in M. Müller et al. (2015), computed for local values of f, N and H for each grid point on the northern and southern boundaries of each region, to obtain bounding dispersion curves.

4 Comparison of simulations to observations

A depth-time comparison between MITgcm48, HYCOM25 and McLane profiler observations of HKE at (43.2°N, 233.7°E) near the Oregon coast (Figure 2) demonstrates that horizontal kinetic energies are high in the upper ocean and lower at depth, consistent with WKB scaling. The vertically-integrated HKE anomaly (Figure 2*d-f*) reveals higher-frequency motions including internal tides. At this location, observed variabil-

This article is protected by copyright. All rights reserved.

Author Manuscript

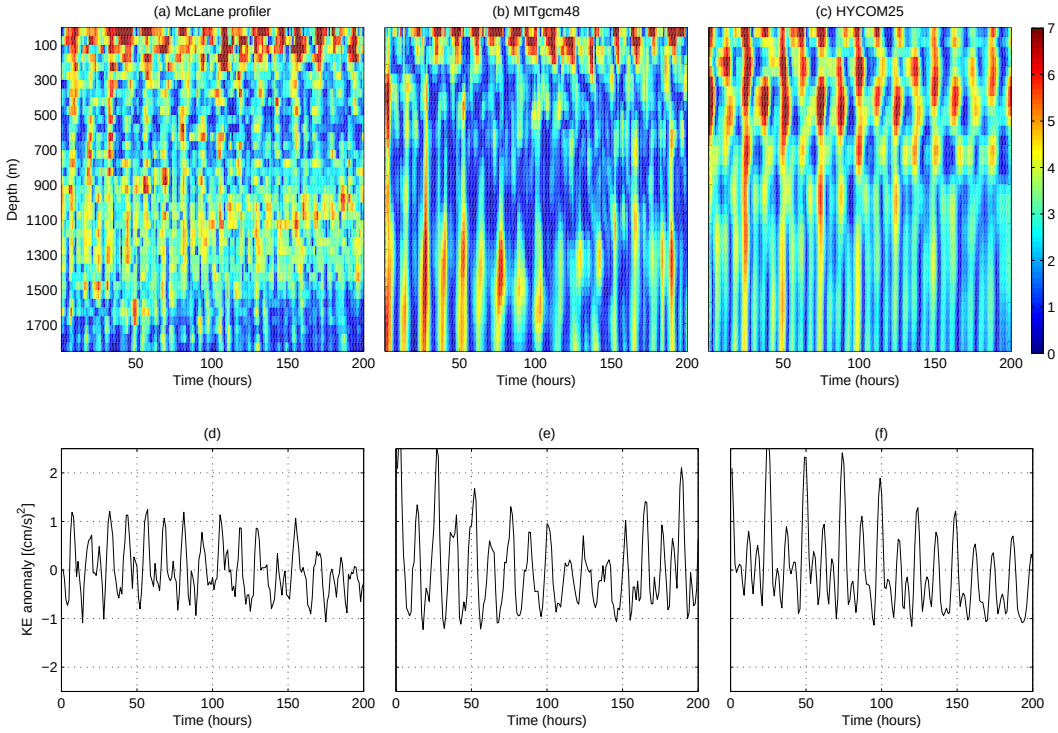


Figure 2. Horizontal kinetic energy HKE ($\mathrm{cm}^2/\mathrm{s}^2$) profile time-series for the first 200 h of each data set (Tables 2 and 3) at (43.2°N, 233.7°E) from (a) a McLane profiler, (b) MITgcm48 and (c) HYCOM25. Time series of vertically averaged HKE anomaly for (d) the McLane profiler, (e) MITgcm48, and (f) HYCOM25.

ity of HKE spans $\sim 1\,(\mathrm{cm/s})^2$, slightly smaller than model variability, but with similar patterns. MITgcm48 exhibits more vertical structure than HYCOM in the upper 200 db or so but, below 200 db, the upper depth cutoff for computing vertical wavenumber spectra, both simulations are clearly missing some of the finer vertical structure seen in observations. The lack of similarity, in terms of the temporal and vertical structures in Figure 2 is partly due to the temporal mismatch between the profiler data and model output (see Table 3). The profiler data starts from September 15, 2005, whereas those of MITgcm48 and HYCOM25 start from October 31, 2011 and January 1, 2014 respectively. However, the dominant motions of near-inertial waves, internal tides, internal gravity waves, and low-frequency motions, which are present at all times are more clearly revealed in spectral plots, as in Figures 3 and 4.

In the remainder of this section, rotary frequency-vertical wavenumber spectra of HKE computed from the nine McLane profilers (see Table 3) are compared with nearest-neighbor grid points in HYCOM25 and MITgcm48. For linear internal waves, CW rotation with depth signifies downward (upward) energy (phase) propagation, while the converse is true for CCW rotation (e.g., Leaman, 1976; MacKinnon et al., 2013b; Alford et al., 2017). Following Alford et al. (2017), $\tilde{u}(z,t)$ is Fourier-transformed in both depth and time resulting in spectra with four quadrants, with positive (negative) vertical wavenumbers indicating upward (downward) energy propagation, and positive (negative) frequencies indicating CCW (CW) rotation in time.

Rotary spectra from McLane profilers, HYCOM25 and MITgcm48 near Hawai'i (28.9°N, 196.5°E) and Luzon Strait (20.9°N, 117.9°E), are displayed in Figure 3. All spectra display asym-

This article is protected by copyright. All rights reserved.

Author Manuscript

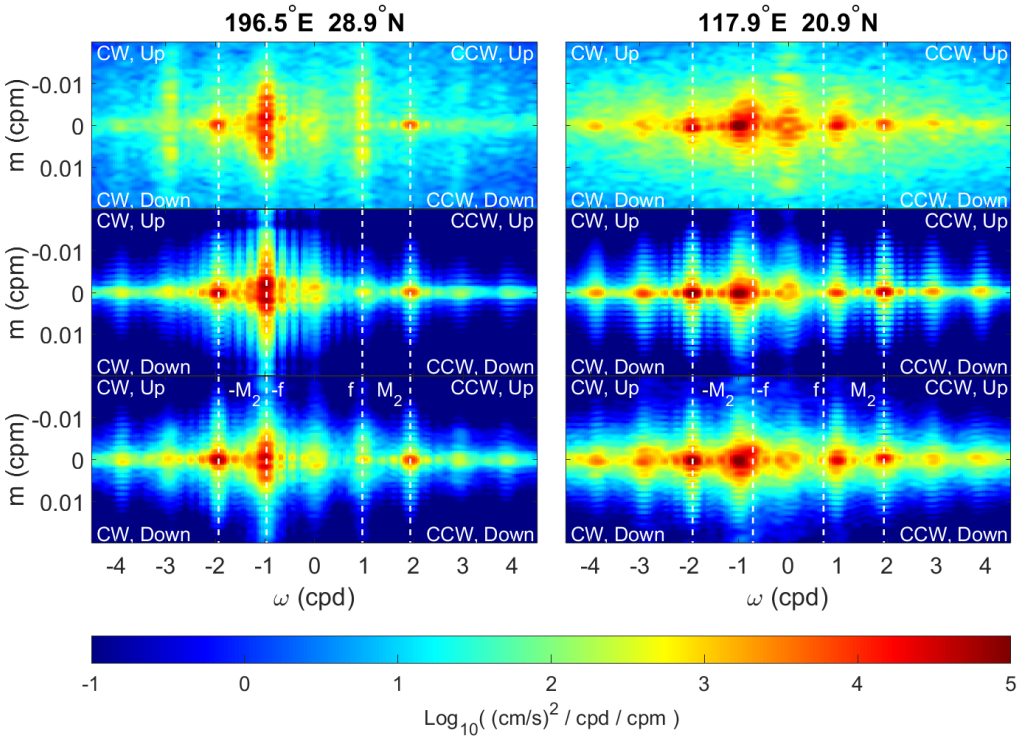


Figure 3. [Row 1] Rotary frequency-vertical wavenumber spectra, $E(\omega, m)\{(\mathrm{cm/s})^2/(\mathrm{cpm\,cpd})\}$ on a $\log_{10}$ scale, of HKE from McLane Profiler time-series at (28.9°N, 196.5°E; left panels) and (20.9°N, 117.9°E; right panels), profilers b and f in Table 3, with HYCOM25 [Row 2] and MITgcm48 [Row 3]. White dashed vertical lines mark the semidiurnal M_2 and inertial frequencies f.

metry between positive and negative frequencies, ω, with more energy in CW-in-time than CCW-in-time as expected in the Northern Hemisphere. Energy in observed spectra are more smoothly spread out in both ω and m, while variance in the models is most strongly concentrated near inertial and tidal frequencies and their overtones. The peaks in both observed and model spectra at overtones of forcing frequencies are consistent with previously derived spectra (e.g., Wunsch, 2016; Savage, Arbic, Alford, et al., 2017). However, as noted in earlier papers (e.g., Arbic et al., 2022, amongst others), the "peakiness" in the overtones is more prominent in models, especially HYCOM, than in observations.

There is less asymmetry between positive and negative m. Observations contain more energy at higher ω and m than models. Observed spectra are smoother in m while models exhibit some bandedness. The bandedness of the model spectra in m is expected due to discretized depth. Higher vertical resolution MITgcm48 exhibits less bandedness than the lower vertical resolution HYCOM25.

Rotary spectra are integrated over all m to derive rotary ω-spectra (Figure 4a,c), and integrated over all ω to derive rotary m-spectra (Figure 4b,d).

CW motions exhibit comparable variance in observations and models for a wide range of ω (Figure 4), with HYCOM25 exhibiting less variance for supertidal ω as seen in other studies (e.g., Savage, Arbic, Alford, et al., 2017; Luecke et al., 2020). At the M_2 frequency of the CW component, the models have relatively large variances compared to the observations. At (28.9°N, 196.5°E), HYCOM25 exhibits higher CW variance than

This article is protected by copyright. All rights reserved.

Author Manuscript

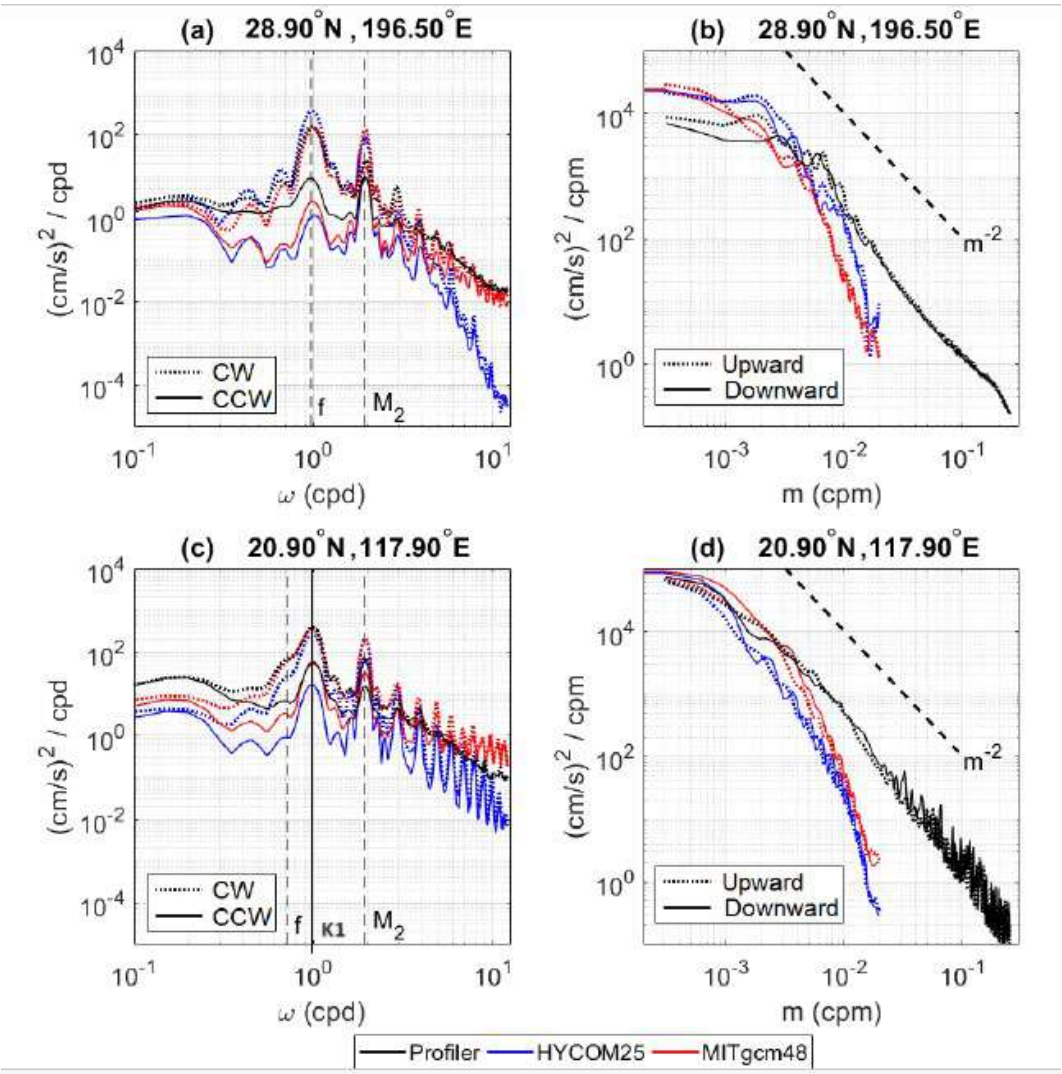


Figure 4. (a) Frequency spectra $E(\omega)$ of horizontal kinetic energy, vertically averaged over 200-1000 m, from McLane Profiler observations (black), MITgcm48 (red) and HYCOM25 (blue), at (28.9°N, 196.5°E). Dotted curves represent clockwise (CW) and bold curves counter-clockwise (CCW) components. (b) As for (a) but vertical wavenumber spectra $E(m)$ integrated over all frequencies. Dotted curves represent upward and bold curves downward components. The absolute values of frequencies and wavenumbers are used on the x-axis. The GM76 (Cairns & Williams, 1976) predicted slope of m^{-2}, appropriate for IGW continuum motions, is depicted by the black dashed line. [(c)-(d)] As for figures (a)-(b) but at (20.9°N, 117.9°E).

This article is protected by copyright. All rights reserved.

Author Manuscript

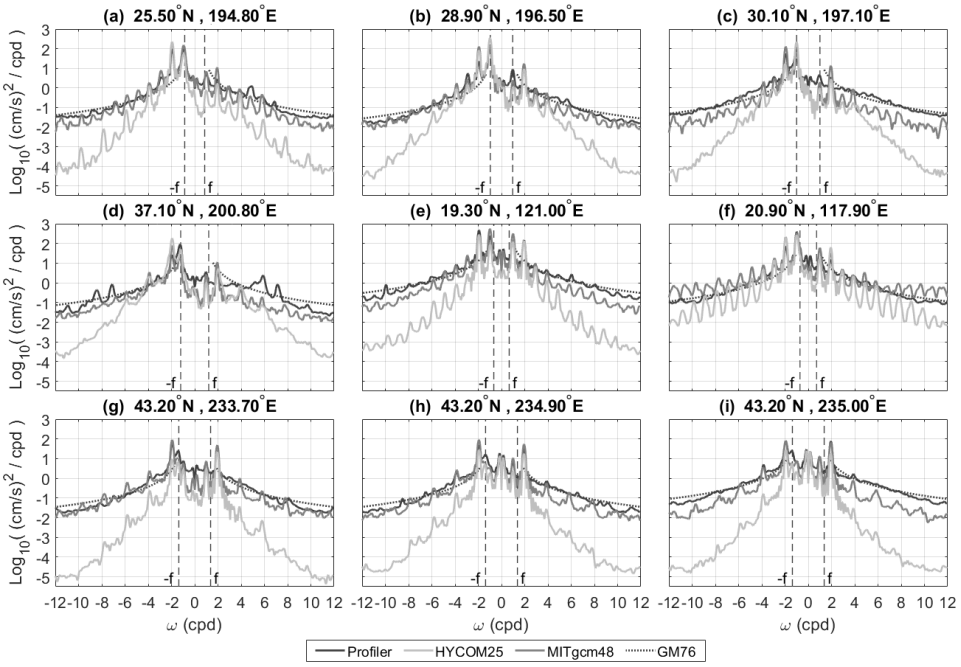


Figure 5. Frequency spectra $E(\omega)$ of HKE, vertically integrated over 200-1000 m, from nine McLane Profiler observations, and nearest-neighbor gridpoints in MITgcm48 and HYCOM25. Predicted slope of GM76 (Cairns & Williams, 1976) is depicted by the dotted curves. Vertical dashed lines depict inertial frequencies f.

both MITgcm48 and the observation around f. For the CCW component of the ω-spectra, the observations have larger variances than the models at almost all frequencies except, for example, around the M_2 frequency where MITgcm48 exceeds HYCOM25 and observations.

Upper-ocean model and observation CW- and CCW-with-depth variances are comparable (Figures 4b,d), implying both exhibit near symmetry in upward and downward energy. This does not necessarily imply symmetry in upward and downward energy-flux because energy-flux also depends on group velocity which in turn is sensitive to horizontal wavenumber (or frequency)(D'Asaro & Perkins, 1984). This contrasts with the global overview of shipboard ADCP measurements in Waterhouse et al. (2022) who reported more downgoing than upgoing energy in the upper 600 m. However, they only examined intermediate wavelengths ($\lambda_z = 50-350$). Model vertical wavenumber spectra resemble those from the mooring profiler at low wavenumbers, but roll off more rapidly for wavelengths smaller than ~ 200 m wavelengths at 196.50°E (Figure 4b) and for wavelengths smaller than ~ 500 m at 117.9°E (Figure 4d). As noted earlier, the regional modeling results of Thakur et al. (2022) suggest that the steep roll-off at higher vertical wavenumbers is due to these global simulations having background KPP turned on.

Integrated ω-spectra for all nine McLane profiler locations follow the predicted GM76 (Cairns & Williams, 1976) model curve closely (Figure 5). MITgcm48 compares well to the observed ω-spectra over a wide range of frequencies at all locations, although it generally has lower variance at higher frequencies than the observations. HYCOM25 compares well to the observations at lower frequencies but exhibits a steeper roll-off at higher frequencies depending on location.

This article is protected by copyright. All rights reserved.

Author Manuscript

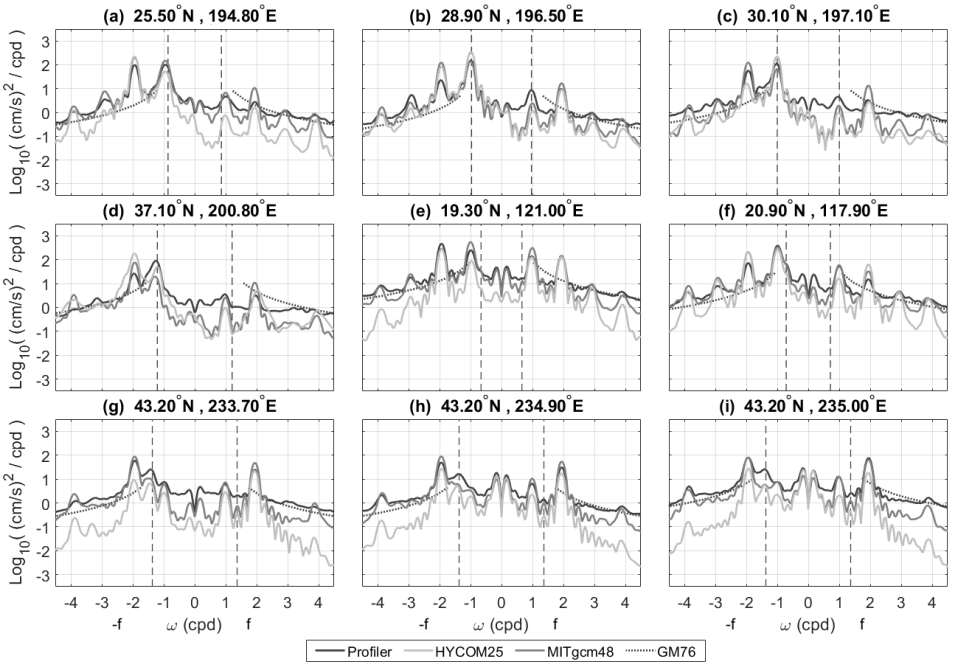


Figure 6. As in Figure 5 but focused on lower frequencies $|\omega| < 4.5f$.

Frequency spectra with a narrower frequency range, focused on lower frequencies ($-4.5 \lesssim \omega \lesssim 4.5\,\mathrm{cpd}$), compare reasonably well to the observations at most locations and match the frequencies of the inertial, tidal and other peaks (Figure 6). HYCOM25 rolls off much faster than MITgcm at some locations (Figure 6g,h,i) along the Oregon coast. The difference between the two models is attributed to their resolutions. MITgcm48 is expected to capture a larger fraction of the frequency spectrum due to its high vertical and horizontal resolution compared to HYCOM25.

Observed vertical wavenumber spectra closely match the GM76 curve at all nine McLane profiler locations (Figure 7; note, however, that the vertical wavenumber spectra shown here include all oceanic motions, not just the IGW motions covered by GM76). The two models lie relatively close to each other except in three locations (Figure $7g, h, i$) corresponding to where their frequency spectra also differ (Figure $6g, h, i$). At all locations, the modeled spectra have a steeper roll-off at higher wavenumbers. In 6 of 9 locations, HYCOM25 exhibits relatively lower vertical wavenumber variance than MITgcm48.

In summary, the global high resolution models capture some of the spectral characteristics in the observed data, with high frequency motions in HYCOM and high vertical wavenumber motions in both models being the motions that are least well modeled. In the remainder of the paper, we describe the frequency-horizontal wavenumber characteristics in the seven regions shown in Figure 1.

5 Horizontal wavenumber-frequency and wavenumber spectra

The horizontal wavenumber-frequency ($K-\omega$) spectra of surface HKE computed from the simulations in all seven regions are described in this section. K denotes the isotropic (radial) wavenumber. After computing the spectra on frequency and two-dimensional horizontal wavenumber (k, l), where k is zonal wavenumber and l is meridional wavenumber, we transfer the spectra to an isotropic wavenumber K in a manner that conserves

This article is protected by copyright. All rights reserved.

Author Manuscript

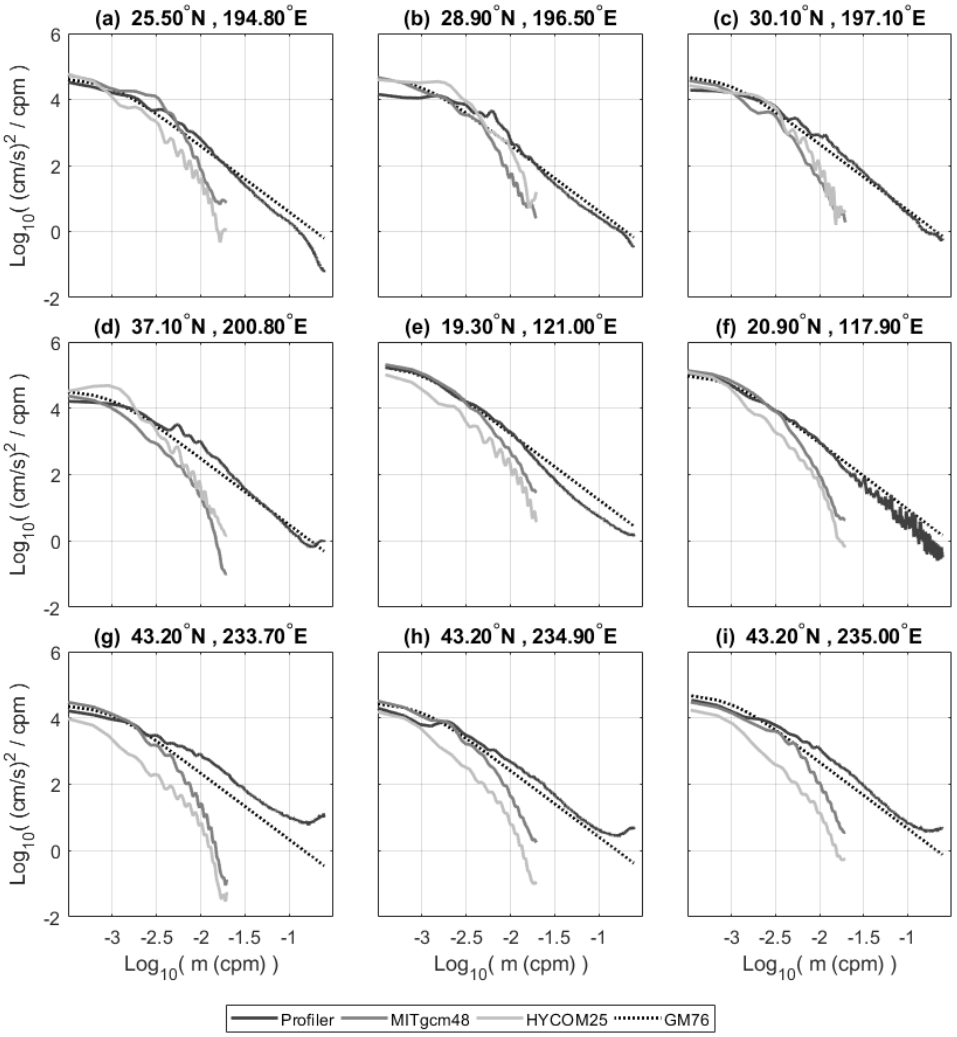


Figure 7. Vertical wavenumber spectra $E(m)$ of horizontal kinetic energy (HKE) integrated over all frequencies over 200-1000 m from nine McLane Profiler observations, and nearest-neighbor gridpoints in MITgcm48 and HYCOM25.

This article is protected by copyright. All rights reserved.

Author Manuscript

energy (Savage, Arbic, Alford, et al., 2017). The isotropic wavenumber K is defined to be an evenly distributed discrete set of wavenumbers whose length is chosen to equal the arithmetic mean of the lengths of k and l (Savage, Arbic, Alford, et al., 2017). Computations use 90 days of hourly time series for both HYCOM and MITgcm (see Table 2). Similarities and differences between the highest resolution simulation in each model and their lower resolution counterparts will be presented. Integrations of $K-\omega$ spectra over different frequency bands will quantify contributions of each band at particular spatial scales. We will also examine how model resolution impacts wavenumber spectra for different frequency bands.

5.1 Horizontal wavenumber-frequency spectra

The horizontal wavenumber-frequency spectra, $E(K, \omega)$, of surface HKE in MITgcm48 is concentrated along the theoretical linear IGW dispersion curves (Figure 8). High variance along the dispersion curves appears to fold back, after reaching the Nyquist frequency of 12 cpd. This aliasing effect, described in Savage, Arbic, Alford, et al. (2017), can be seen in all regions in MITgcm48 though less prominent in the North Atlantic (Figure 8*c*) likely due to the increased activity of eddies blurring out the IGW variance off dispersion curves (also see Holloway (1983)). Regions with high internal wave activity display more focused and high variances along the dispersion curves (e.g. Figures 8*b*, *d*, *g*) while regions with increased mesoscale activity such as the Kuroshio (Figure 8*a*) and North Atlantic (Figure 8*c*) display larger spectral densities at lower frequencies and horizontal wavenumbers. Larger variances appearing as horizontal stripes at ~ 2 cpd in each region are indicative of prominence of semidiurnal tide, the largest tide in the ocean.

Aliasing observed in most regions in MITgcm48 is less prominent in HYCOM25, except in the Indian Ocean and (faintly) in the North Pacific (Figure 9). This suggests that MITgcm48 better resolves the IGW surface HKE spectrum than HYCOM25 at high frequencies and wavenumbers, due to its higher horizontal and vertical resolution. MITgcm48 and HYCOM25 both exhibit high variances at low frequencies and wavenumbers in the Kuroshio though the North Atlantic in HYCOM25 displays less intense KE variance than MITgcm48 at the lower-frequency and lower-wavenumber end of the spectrum. The spectral density at the low-frequency and low-wavenumber end in the South Pacific is more prominent in HYCOM25 than MITgcm48.

Within both MITgcm and HYCOM, increasing model resolution results in a more energetic IGW continuum (Figure 10) as previously reported (M. Müller et al., 2015; Savage, Arbic, Alford, et al., 2017; Luecke et al., 2020). This finding is especially obvious from the rays of high variance along the bounding dispersion curves which extend to higher frequencies and wavenumbers with increasing resolution in both MITgcm (Figure 10, left panels) and HYCOM (Figure 10, right panels). The high spectral density along the dispersion curves is more focused in separate vertical modes in MITgcm24 than HYCOM25 (middle panels in Figure 10). The HYCOM25 spectral densities appear more energetic in lower wavenumbers and frequencies than MITgcm24 in the North Pacific, similar to the findings in Savage, Arbic, Alford, et al. (2017) for SSH variance (see their Figure 6*c*, *d*). The horizontal wavenumber-frequency spectra of surface HKE for the other MITgcm and HYCOM simulations in other regions show qualitatively similar features (not shown).

5.2 Frequency-band contributions to KE horizontal wavenumber spectra

Recently, there has been renewed interest in quantifying the relative strengths of low-frequency eddy and high-frequency internal wave motions in the ocean (Richman et al., 2012; Callies & Ferrari, 2013; Rocha et al., 2016a, 2016b; Savage, Arbic, Richman, et al., 2017; Savage, Arbic, Alford, et al., 2017; Qiu et al., 2017, 2018; Torres et al., 2018; Lien & Sanford, 2019; C. Wang et al., 2023; J. Wang et al., 2019, and references therein,

This article is protected by copyright. All rights reserved.

Author Manuscript

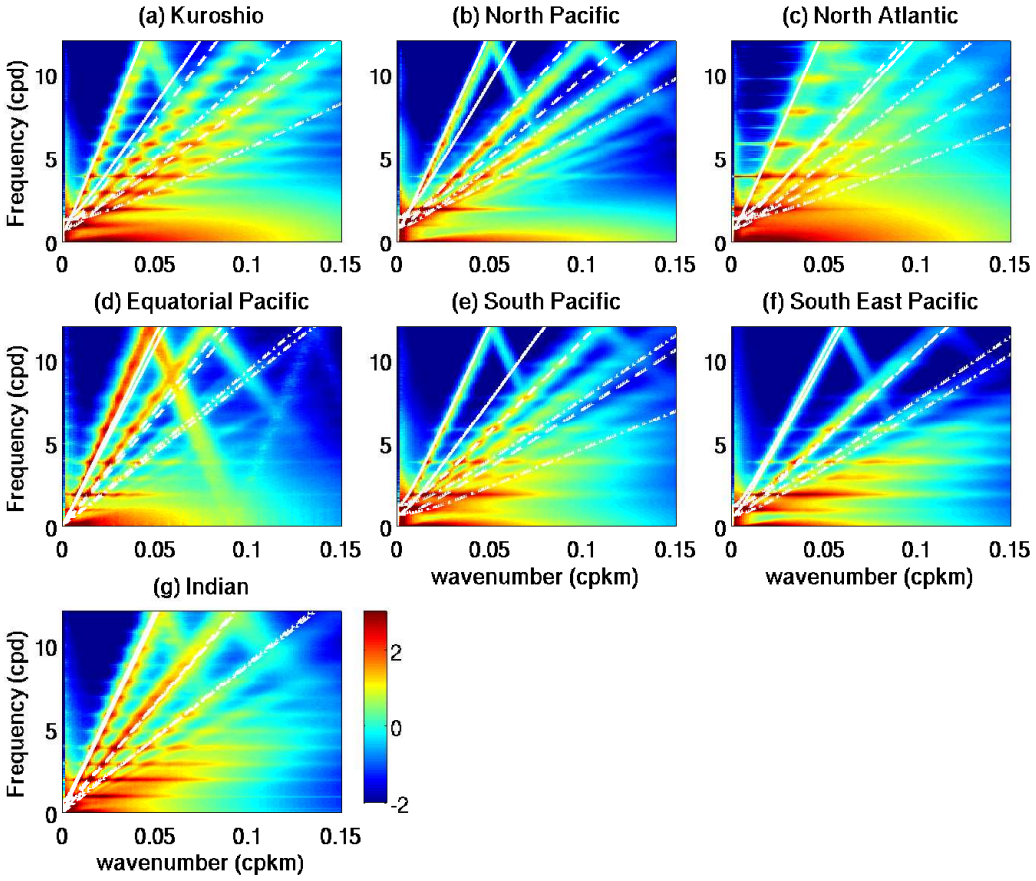


Figure 8. Horizontal wavenumber-frequency spectra of surface HKE, $E(K,\omega)\,\{(\mathrm{cm/s})^2/(\mathrm{cpkm\,cpd})\}$ on a $\log_{10}$ scale, across seven regions (see Figure 1) in MIT-gcm48. As described in section 3, white curves show bounding linear dispersion relations of the first (solid), second (dashed) and third (dashed-dotted) vertical modes as in M. Müller et al. (2015).

This article is protected by copyright. All rights reserved.

Author Manuscript

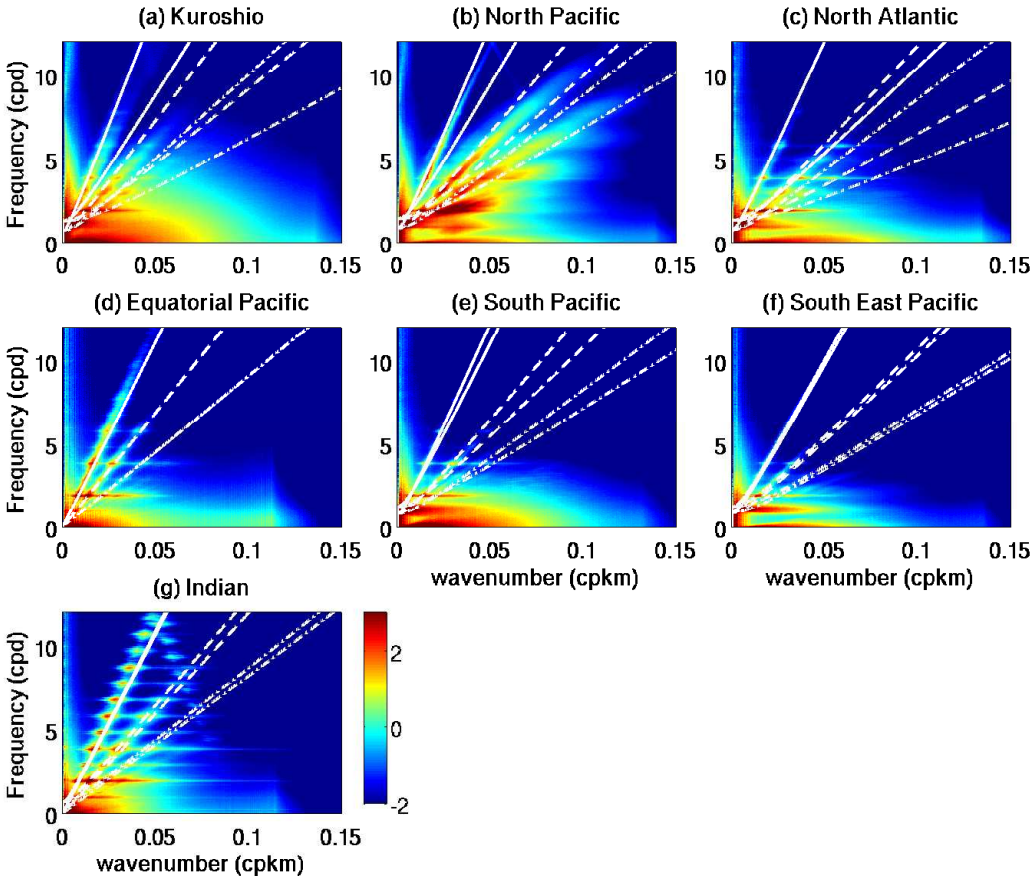


Figure 9. As in Figure 8 but for HYCOM25.

This article is protected by copyright. All rights reserved.

Author Manuscript

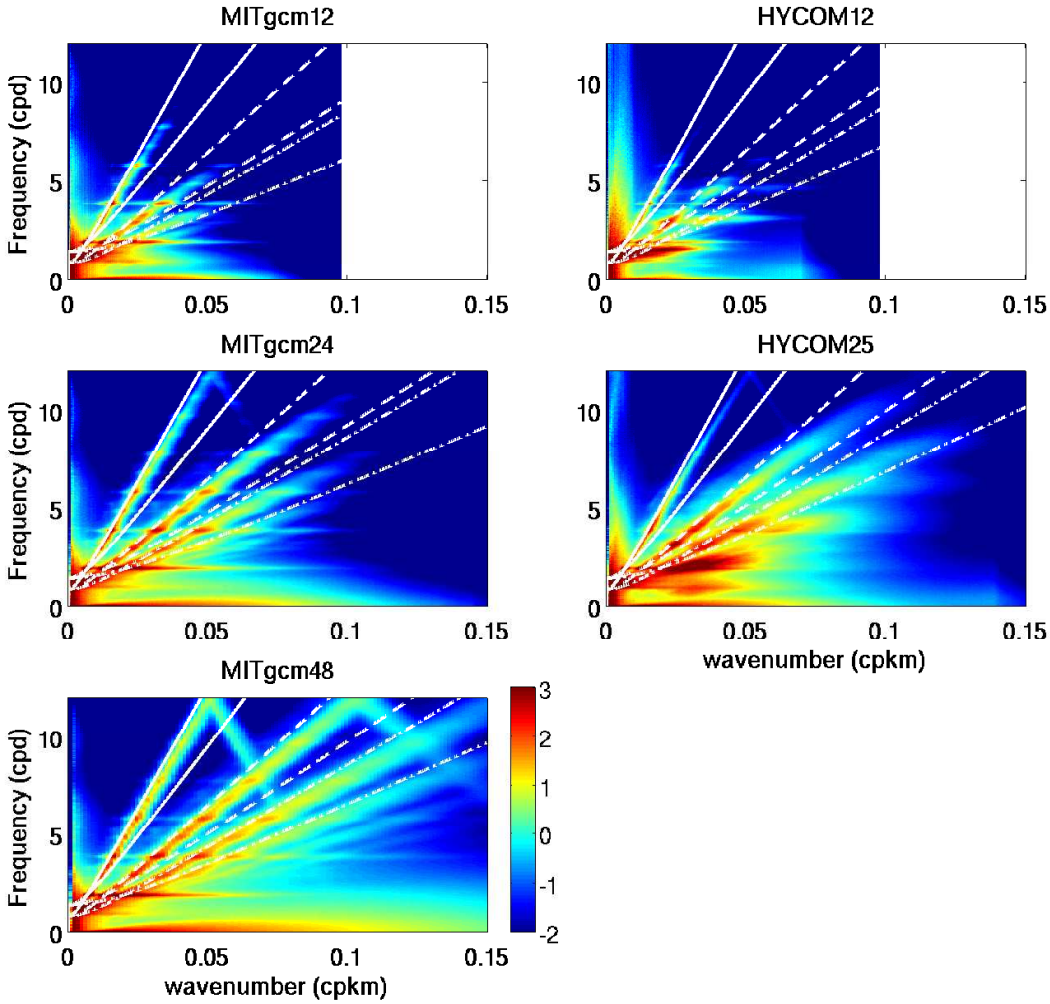


Figure 10. Horizontal wavenumber-frequency spectra of surface HKE, $E(K,\omega)\,\{(\mathrm{cm/s})^2/(\mathrm{cpkm\,cpd})\}$ on a $\log_{10}$ scale, for the North Pacific region in all five simulations. The white curves show the bounding linear dispersion relations of the first (solid), second (dashed) and third (dashed-dotted) vertical modes, computed as in M. Müller et al. (2015).

This article is protected by copyright. All rights reserved.

Author Manuscript

among others) because of the recently launched SWOT mission (Fu et al., 2012; Morrow et al., 2019), which is measuring two-dimensional sea surface height at high resolution. Before these recent efforts to try to distinguishing geostrophic and quasi-geostrophic motions and internal waves, there have been previous attempts (P. Müller et al., 1988; Kunze & Sanford, 1993; Kunze, 1993). At the smaller scales (higher wavenumbers) to be measured by SWOT, high-frequency IGW motions are expected to be a significant signal. Motivated by this, we integrate the horizontal wavenumber-frequency surface HKE spectra over low-frequency $\omega < 0.70\,\mathrm{cpd}$, semidiurnal $1.86 < \omega < 2.05\,\mathrm{cpd}$, diurnal $0.87 < \omega < 1.05\,\mathrm{cpd}$, near-inertial wave plus diurnal (NIW+diurnal) and supertidal $\omega > 2.05\,\mathrm{cpd}$ bands, to ascertain their contributions to horizontal wavenumber spectral density. The low-frequency band is mixed in with near-inertial wave motions (NIW) in the equatorial Pacific and Indian regions, but is sub-inertial in the five non-equatorial regions. Because near-inertial motions and diurnal tides overlap off equator we denote the frequency band that includes both signals as "NIW+diurnal". This band is computed by integrating from $0.9f_s$ to $1.1f_n$, where f_s and f_n are the values of f at the southern and northern boundaries of the regions, respectively. Diurnal tides can be separated from NIW and low-frequency motions in the equatorial regions, so the "diurnal band" applies only to equatorial regions. (See Qiu et al. (2018) for a different method for separating eddy and IGW flows.)

The horizontal wavenumber spectra of MITgcm48 surface HKE integrated over the different frequency bands is displayed in Figure 11. In most non-equatorial regions, the low-frequency and NIW+diurnal bands dominate at low wavenumbers (scales $\gtrsim 100\,\mathrm{km}$). In the North Atlantic, semi-diurnal tides are also prominent at low wavenumbers. Similarly, low-frequency motions are prominent at low wavenumbers in equatorial regions (Figures 11*f*-*g*). The supertidal band contributes little at low wavenumbers (large scales), but is significant at high wavenumbers (scales $\lesssim 50\,\mathrm{km}$; see especially Figures 11*d*-*g*). The supertidal influence on high wavenumbers is especially prominent in the equatorial Indian ocean (Figure 11*g*). The prominence of supertidal motions in equatorial regions can be seen in global maps of high-frequency SSH and surface HKE in Savage, Arbic, Richman, et al. (2017) and Solano et al. (2023), respectively. These conclusions about the greater role of supertidal motions for smaller-scale kinetic energy are qualitatively similar to those in Qiu et al. (2018) with the caveat that our definitions are somewhat different. In most regions, semidiurnal tides have large KE variance ($\gtrsim 10^4\,(\mathrm{cm/s})^2/\mathrm{cpkm}$) around $4\times\left(10^{-3}-10^{-2}\right)$ cpkm, except in the North Atlantic region where this range is wider ($\sim 30-2000\,\mathrm{km}$). The wiggles seen in the semidiurnal and supertidal curves are due to aliasing (section 5.1), because the reflected rays in spectral density influence these two frequency bands. In equatorial regions (Figure 11*f*-*g*), diurnal motions dominate over semidiurnal and supertidal motions at low wavenumbers. As discussed in Arbic et al. (2022), diurnal surface HKE likely contains significant non-tidal as well as tidal motions.

Increased resolution yields large increases in high-horizontal-wavenumber variance, across all frequency bands including the supertidal band (Figure 12). At high wavenumbers, simulations with similar resolutions tend to lie close together, with MITgcm48 exhibiting the largest variance. The large increases at the high wavenumber spectrum with increased resolution imply that the models have not yet achieved numerical convergence. Thus, quantitative conclusions about the relative importance of high-frequency semidiurnal and supertidal motions versus low-frequency motions based on computations from any of these simulations must be treated with caution.

The spectral energy level in each high-frequency band relative to the low-frequency band depends strongly on region, model (HYCOM vs. MITgcm), and the horizontal resolution within each model (Figure 13d). Thus, the transition length scale for separating low-frequency eddy and high-frequency internal wave motions depends on the model employed, and the resolution (grid spacing) employed in that model. Low-frequency mo-

This article is protected by copyright. All rights reserved.

Author Manuscript

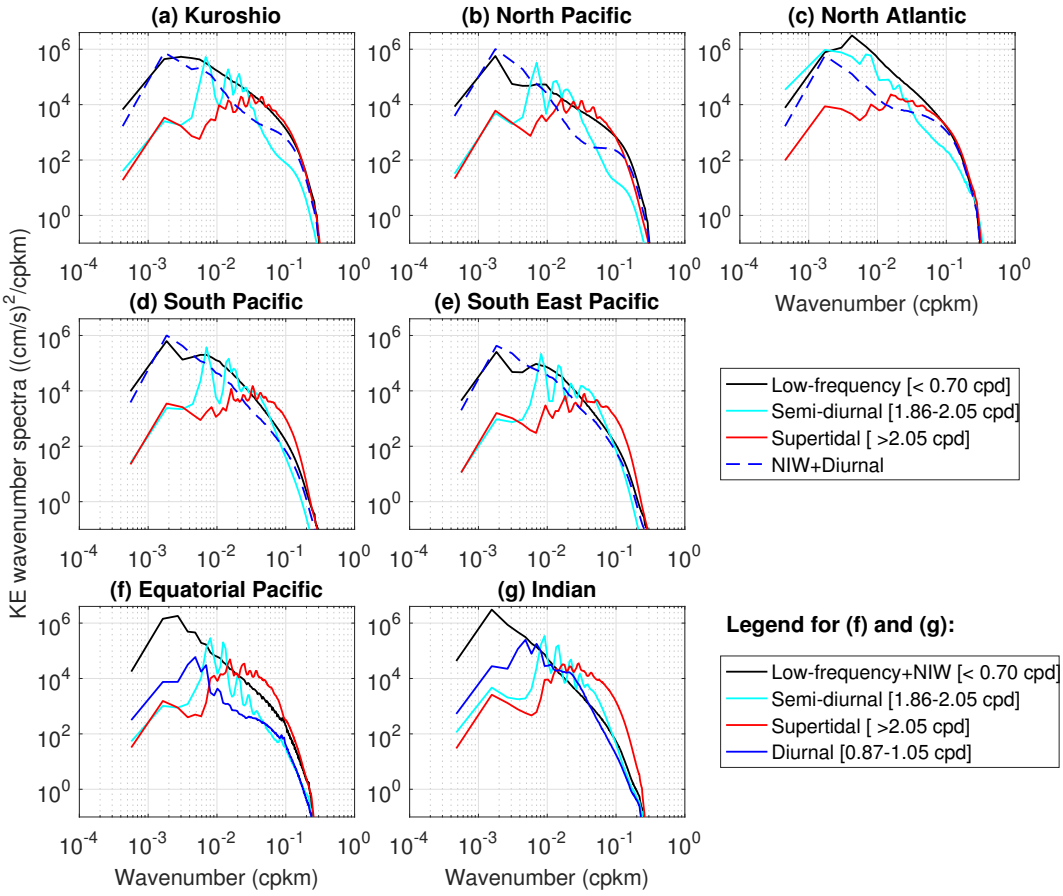


Figure 11. Horizontal wavenumber spectra of surface HKE in all regions in MITgcm48 (see Figures 1 and 8) integrated over frequency bands indicated in the legends.

This article is protected by copyright. All rights reserved.

Author Manuscript

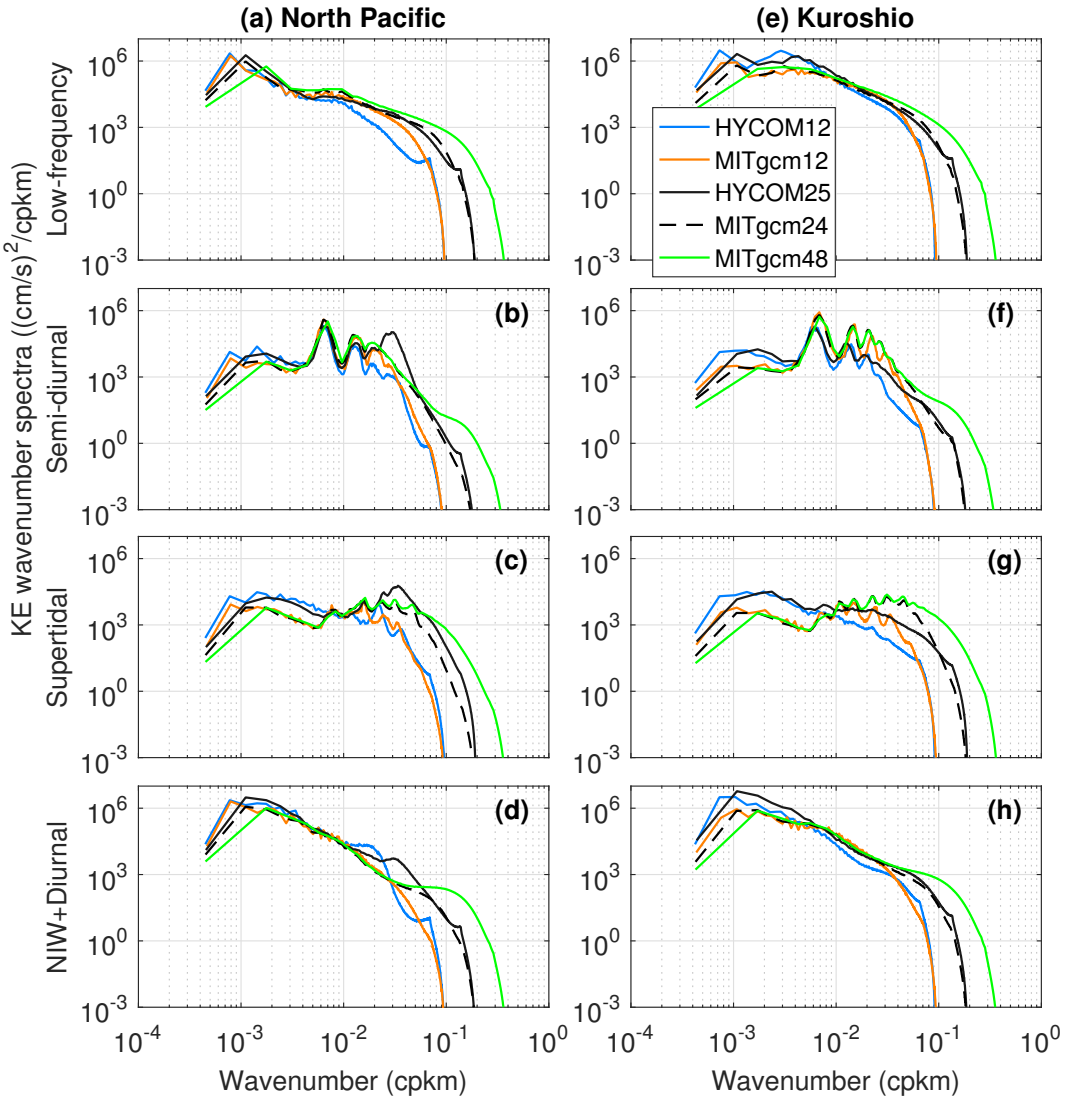


Figure 12. Horizontal wavenumber spectra of surface HKE in North Pacific (left column) and Kuroshio (right column) regions integrated over low-frequency (**a** and **e**), semi-diurnal (**b** and **f**), supertidal (**c** and **g**), and NIW+diurnal bands (**d** and **h**) in all five simulations.

This article is protected by copyright. All rights reserved.

Author Manuscript

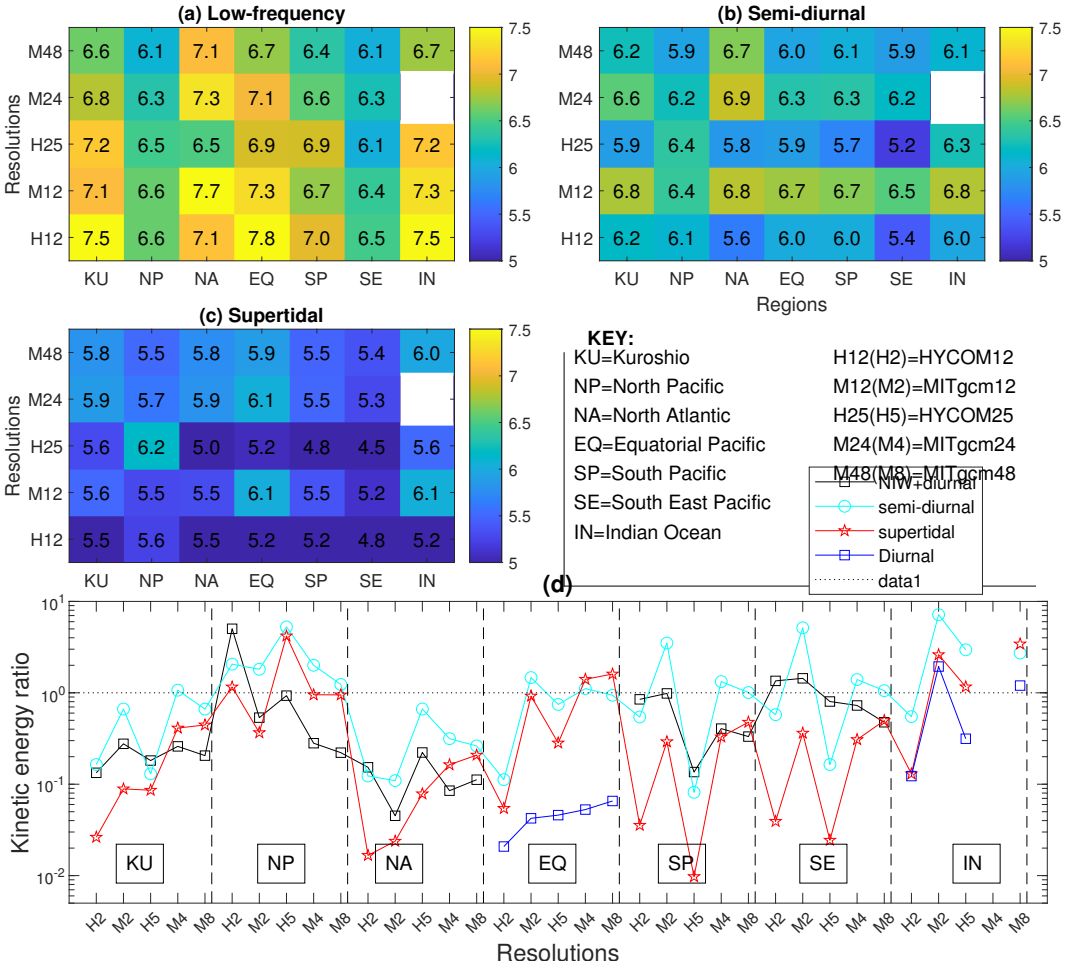


Figure 13. [(a)-(c)] Surface HKE (cm^2/s^2 in $\log_{10}$ scale) integrated over all horizontal wavenumbers and over (a) low-frequency, (b) semi-diurnal and (c) supertidal bands, in all regions (horizontal axis) and simulations (vertical axis). The white spaces indicate absence of output for the Indian Ocean in MITgcm24. (d) Ratio of high wavenumber ($\geq 10^{-2}$ cpkm) integrated spectral surface HKE in different high-frequency bands to integrated low-frequency band surface HKE.

tions generally contain the largest amount of energy, and supertidal motions the least (Figure 13a-c). High horizontal wavenumber (wavenumbers greater than about 10^{-2} cpkm) energy in each high-frequency band (Figure 13d) is comparable to (and some times greater than) energy in the low-frequency band. In the North Pacific in particular, all five simulations have a high-wavenumber semi-diurnal tide with greater energy than high-wavenumber low-frequency motions. Most simulations predict the South East Pacific to have comparatively large energy in the NIW+diurnal band. High-wavenumber energy in the diurnal band in the Equatorial Pacific is much lower than that in the Indian Ocean.

6 Summary and Look-Ahead

This paper makes two main points about internal gravity waves (IGWs) and other oceanic motions in high-resolution global simulations of HYCOM and MITgcm that are forced simultaneously by atmospheric fields and astronomical tidal potential, and that have been shown to partially resolve the supertidal internal gravity wave (IGW) contin-

This article is protected by copyright. All rights reserved.

Author Manuscript

uum spectrum. First, horizontal wavenumber-frequency spectra demonstrate that the amount of surface horizontal kinetic energy (HKE) in higher-frequency internal tide and IGW motions relative to the amount in lower-frequency eddying motions is sensitive to the model (here, HYCOM vs. MITgcm) and to the horizontal grid spacings employed in the simulations. Therefore, quantitative predictions about the relative strength of low-frequency eddy vs. high-frequency IGW motions made from global IGW models should be treated with some care. The relative strength of low-frequency eddy vs. high-frequency IGW motions is a first-order issue for the SWOT mission, which is measuring SSH at high horizontal resolution and in two dimensions, but at a temporal resolution that is insufficient for separating low-frequency vs. high-frequency motions. Second, a comparison of the vertical wavenumber spectra in currently available global IGW models with moored McLane profilers reveals that the spectrum in models rolls off too steeply at high vertical wavenumbers, making this an important target for further improvement in models of IGWs and other oceanic motions.

We present the IGW surface HKE horizontal wavenumber-frequency spectra in seven regions of the world ocean. Two simulations of global HYCOM with horizontal grid spacings of 1/12.5° (HYCOM12) and 1/25° (HYCOM25), and three simulations of global MITgcm with horizontal grid spacings of 1/12° (MITgcm12), 1/24° (MITgcm24) and 1/48° (MITgcm48) are analyzed. In the horizontal wavenumber-frequency surface HKE spectra, high KE variance aligns along theoretical IGW dispersion curves as reported in earlier analyses of sea surface height (SSH) and surface HKE variance in both HYCOM (M. Müller et al., 2015; Savage, Arbic, Alford, et al., 2017) and MITgcm (Rocha et al., 2016a, 2016b; Savage, Arbic, Alford, et al., 2017; Torres et al., 2018; J. Wang et al., 2019). Dispersion curves of high surface HKE are prominent in regions of high IGW activity such as the North Pacific, Equatorial Pacific and Indian Oceans but less obvious in eddying regions such as the North Atlantic (Figures 8 and 9). In addition, high variance along the bounding dispersion curves is more prominent and focused in MITgcm48 than HYCOM25, demonstrating that increasing model resolution is important for resolving high-frequency IGWs in global models. Increasing model resolution generally yields a more energetic IGW continuum.

Frequency-vertical wavenumber spectra of horizontal kinetic energy (HKE) from HYCOM25 and MITgcm48 compare well to nine McLane profiler observations at low vertical wavenumbers (Figure 4). In both models and observations, there is near symmetry in positive and negative vertical wavenumber, implying equal downward and upward propagating energy in the upper 200−1000 m of the pycnocline. However, this does not imply that vertical energy-fluxes are symmetric because vertical energy-flux depends not only on energy but also on group velocity which is sensitive to frequency (or horizontal wavenumber) at low frequencies. For example, D'Asaro and Perkins (1984) showed that, even though there was more clockwise-with-depth (downgoing) than counterclockwise-with-depth (upgoing) near-inertial energy, upgoing energy-flux was comparable to downgoing because the former was associated with shorter horizontal wavelengths. These results contrast with those of Pinkel (1985), Waterhouse et al. (2022) and Kunze et al. (2023) who have reported more downgoing than upgoing energy in the upper ocean. At low frequencies, both models compare reasonably well to observed spectra. However, MITgcm48 is comparable to observations over a wider range of frequency than HYCOM25. The deficiency of HYCOM spectra at supertidal frequencies has been seen in other studies (e.g., Savage, Arbic, Alford, et al., 2017; Luecke et al., 2020). The vertical wavenumber spectra of HKE from both models rolls off much faster than the observations (Figure 7), but differences between HYCOM and MITgcm are not nearly as pronounced as they are in frequency domain. Turning off background KPP settings in regional MITgcm simulations yields vertical wavenumber spectra in closer agreement with observations (Thakur et al., 2022). Future global IGW simulations will likewise attempt to shut off KPP so that vertical wavenumber spectra do not roll off as steeply. For instance, vertical wavenumbers, horizontal wavenumbers, and frequencies of IGWs are related to each other through

This article is protected by copyright. All rights reserved.

Author Manuscript

the internal wave dispersion relation. It is possible therefore that our explorations of KPP and the vertical wavenumber spectra will connect to the horizontal wavenumber spectra that are also discussed here. However, we save a more detailed examination of these connections for future work.

As model resolution continues to improve, at some point nonhydrostatic processes will affect spectra and other dynamical quantities of IGWs. Nonhydrostatic effects come into play when horizontal and vertical grid spacings are comparable; this is extremely expensive computationally. Nonhydrostatic effects are seen at frequencies near the buoyancy frequency N, which in the pycnocline is much greater than the near-inertial and semidiurnal frequencies; the latter frequencies contain most of the IGW energy and even a substantial amount of IGW shear (Alford, 2010). There is little observational guidance on near-N waves, and the global models examined here are far from the order-one aspect ratio limit. We are just beginning to explore nonhydrostatic effects in regional IGW simulations so it is too early to say whether we will be able to infer any differences from our hydrostatic simulations with the computational power presently available.

7 Open research

MITgcm LLC4320 output is available from the ECCO Data Portal as described in Abernathey (2019). Global HYCOM25 output can be accessed via the OSiRIS infrastructure (OSiRIS, 2024). Profile data from the McLane profilers and corresponding profiles from HYCOM and MITgcm can be downloaded from Savage and Arbic (2017). The Matlab code used to process the MITgcm LLC4320 and HYCOM outputs into the results used in this paper, the results from MITgcm and HYCOM and the code used to produce the surface HKE and integrated plots in the paper, are provided in Ansong and Arbic (2023).

Acknowledgments

We acknowledge the editor and two anonymous reviewers, whose useful comments greatly improved the presentation of our results. BKA thanks Carl Wunsch for his useful class notes on internal gravity wave dispersion relations, and useful conversations on internal gravity wave spectra, internal wave modeling, and much else. We thank the technical teams, captains, and crews of the various ships that deployed and recovered the McLane profilers. We also acknowledge the United States Office of Naval Research (ONR) and National Science Foundation (NSF) for the support that enabled deployment of the McLane profilers.

JKA, ACS and BKA acknowledge funding from the University of Michigan Associate Professor Support Fund, supported by the Margaret and Herman Sokol Faculty Awards. JKA, ACS and BKA gratefully acknowledge support from National Science Foundation (NSF) grant OCE-0968783 and Office of Naval Research (ONR) grants N00014-11-1-0487 and N00014-15-1-2288. The NSF grant was part of a multi-institution Climate Process Team grant, led by Professor Jennifer MacKinnon of UCSD. MHA acknowledges funding provided by the Office of Naval Research's Task Force Ocean program under award N00014-19-1-2635. EK acknowledges support from ONR grant N00014-18-1-2598. JFS and AJW were supported by the projects "Eddy resolving global ocean prediction including tides" and"Ageostrophic vorticity dynamics" sponsored by the ONR under program element 0602435N, and by N00014-11-1-2288. ACS acknowledges funding provided by the National Aeronautics and Space Administration (NASA) Earth and Space Science Fellowship grant NNX16AO23H. ACS, BKA, ADN, and JFS also acknowledge funding from NASA grants NNX13AD95G, NNX16AH79G, NNX17AH55G, and 80NSSC20K1135.

This work was supported in part by a grant of computer time from the Department of Defense (DoD) High Performance Computing Modernization Program at the Navy

This article is protected by copyright. All rights reserved.

Author Manuscript

DoD Supercomputing Resource Center. This research was made possible, in part, by the OSiRIS project at University of Michigan and by computing resources provided by the NASA Advanced Supercomputing (NAS) Division of the Ames Research Center. DM carried out research at the Jet Propulsion Laboratory, California Institute of Technology, under contract with NASA, with support from the Physical Oceanography and Modeling, Analysis, and Prediction Programs. This is NRL contribution NRL/JA/7320-23-6165 and has been approved for public release.

References

Abernathey. (2019). *Petabytes of Ocean Data, Part 1: NASA ECCO Data Portal* [Blog post]. Retrieved from `https://medium.com/pangeo/petabytes-of-ocean-data-part-1-nasa-ecco-data-portal-81e3c5e077be`

Alford, M. H. (2010). Sustained, full-water-column observations of internal waves and mixing near Mendocino Escarpment. *Journal of Physical Oceanography*, *40*. doi: 10.1175/2010JPO4502.1

Alford, M. H., MacKinnon, J., Zhao, Z., Pinkel, R., Klymak, J., & Peacock, T. (2007). Internal waves across the Pacific. *Geophysical Research Letters*, *34, L24601*, 1-6. doi: 10.1029/2007GL031566

Alford, M. H., Mackinnon, J. A., Nash, J. D., Simmons, H. L., Pickering, A., Klymak, J. M., ... Lu, C.-W. (2011). Energy flux and dissipation in Luzon Strait: Two tales of two ridges. *Journal of Physical Oceanography*, *41*, 2211-2222.

Alford, M. H., Mackinnon, J. A., Pinkel, R., & Klymak, J. M. (2017). Space-time scales of shear in the north pacific. *Journal of Physical Oceanography*. doi: 10.1175/JPO-D-17-0087.1

Ansong, J. K., & Arbic, B. K. (2023). *Dataset of surface and sub-subsurface internal gravity wave kinetic energy spectra from global ocean models and observations [Data set]*. University of Michigan - Deep Blue Data. `https://doi.org/10.7302/459w-xb52`.

Ansong, J. K., Arbic, B. K., Buijsman, M. C., Alford, M. H., Zhao, Z., Harper, L., ... Wallcraft, A. J. (2017). Semidiurnal internal tide energy fluxes and their variability in a global ocean model and moored observations. *Journal of Geophysical Research Oceans*, *122 (3)*, 1882-1900. doi: 10.1002/2016JC012184

Ansong, J. K., Arbic, B. K., Buijsman, M. C., Richman, J. G., Shriver, J. F., & Wallcraft, A. J. (2015). Indirect evidence for substantial damping of low-mode internal tides in the open ocean. *Journal of Geophysical Research Oceans*, *120*, 6057-6071. doi: 10.1002/2015JC010998

Arbic, B. K. (2022). Incorporating tides and internal gravity waves within global ocean general circulation models: A review. *Progress in Oceanography*, *206*, 102824. doi: 10.1016/j.pocean.2022.102824

Arbic, B. K., Alford, M. H., Ansong, J. K., Buijsman, M. C., Ciotti, R. B., Farrar, J. T., ... Zhao, Z. (2018). A primer on global internal tide and internal gravity wave continuum modeling in HYCOM and MITgcm. In *New Frontiers in Operational Oceanography* (eds. E. Chassignet, A. Pascual, J. Tintore, and J. Verron) (p. 307-392). GODAE OceanView. doi: 10.17125/gov2018.ch13

Arbic, B. K., Elipot, S., Brasch, J. M., Menemenlis, D., Ponte, A. M., Shriver, J. F., ... Nelson, A. D. (2022). Near-surface oceanic kinetic energy distributions from drifter observations and numerical models. *Journal of Geophysical Research: Oceans*, *127*, e2022JC018551. doi: 10.1029/2022JC018551

Arbic, B. K., Richman, J. G., Shriver, J. F., Timko, P. G., Metzger, E. J., & Wallcraft, A. J. (2012). Global modeling of internal tides within an eddying ocean general circulation model. *Oceanography*, *25 (2)*, 20-29.

Arbic, B. K., Wallcraft, A. J., & Metzger, E. J. (2010). Concurrent simulation of the eddying general circulation and tides in a global ocean model. *Ocean Modelling*, *32*, 175-187.

This article is protected by copyright. All rights reserved.

Author Manuscript

Barkan, R., Winters, K. B., & McWilliams, J. C. (2017). Stimulated imbalance and the enhancement of eddy kinetic energy dissipation by internal waves. *Journal of Physical Oceanography*, *47*, 181-198. doi: 10.1175/JPO-D-16-0117.s1

Bleck, R. (2002). An oceanic general circulation model framed in hybrid isopycnic-Cartesian coordinates. *Ocean Modelling*, *37*, 55-88.

Buijsman, M. C., Ansong, J. K., Arbic, B. K., Richman, J. G., Shriver, J. F., Timko, P. G., ... Zhao, Z. (2016). Impact of internal wave drag on the semidiurnal energy balance in a global ocean circulation model. *Journal of Physical Oceanography*, *46*, 1399-1419. doi: 10.1175/JPO-D-15-0074.1

Buijsman, M. C., Stephenson, G. R., Ansong, J. K., Arbic, B. K., Green, J. A. M., Richman, J. G., ... Zhao, Z. (2020). On the interplay between horizontal resolution and wave drag and their effect on tidal baroclinic mode waves in realistic global ocean simulations. *Ocean Modelling*, *152*, 101656. doi: 10.1016/j.ocemod.2020.101656

Cairns, J. L., & Williams, G. O. (1976). Internal wave observations from a midwater float. *Journal of Geophysical Research*, *81 (12)*, 1943-1950. doi: 10.1029/JC081i012p01943

Callies, J., & Ferrari, R. (2013). Interpreting energy and tracer spectra of upper-ocean turbulence in the submesoscale range (1-200 km). *Journal of Physical Oceanography*, *43*, 2456-2474. doi: 10.1175/JPO-D-13-063.1

Chassignet, E. P., Hurlburt, H. E., Metzger, E. J., Smedstad, O. M., Cummings, J. A., Halliwell, G. R., ... Wilkin, J. (2009). Global ocean prediction with the HYbrid Coordinate Ocean Model (HYCOM). *Oceanography*, *22*, 64–76.

D'Asaro, E., & Perkins, H. (1984). A near-inertial internal wave spectrum for the Sagaso Sea in late summer. *Journal of Physical Oceanography*, *14*, 489-505.

Dee, D. P., Uppala, S. M., Simmons, A. J., Berrisford, P., Poli, P., Kobayashi, S., ... Vitart, F. (2011). The ERA-interim reanalysis: Configuration and performance of the data assimilation system. *Quarterly Journal of The Royal Meteorological Society*, *137*, 553–597. doi: 10.1002/qj.828

de Lavergne, C., Madec, G., Le Sommer, J., Nurser, A., & Garabato, A. (2016). The impact of a variable mixing efficiency on the abyssal overturning. *Journal of Physical Oceanography*, *46(2)*, 663-681. doi: 10.1175/JPO-D-14-0259.1

Delpech, A., Barkan, R., Srinivasan, K., McWilliams, J. C., Arbic, B. K., Siyanbola, O. Q., & Buijsman, M. C. (2024). Eddy-internal wave interactions and their contribution to cross-scale energy fluxes: A case study in the California Current. *Journal of Physical Oceanography*, *54*, 741–754. doi: https://doi.org/10.1175/JPO-D-23-0181.1

Doherty, K. W., Frye, D. E., Liberatore, S. P., & Toole, J. M. (1999). A moored profiling instrument. *Journal of atmospheric and ocean technology*, *16*, 1816–1829. doi: http://dx.doi.org/10.1175/1520-0426(1999)016⟨1816:AMPI⟩2.0.CO;2

Dushaw, B. D., Worcester, P. F., Cormuelle, B. D., Howe, B. M., & Luther, D. S. (1995). Baroclinic and barotropic tides in the central North-Pacific Ocean determined from long-range reciprocal acoustic transmissions. *Journal of Physical Oceanography*, *25*, 631-647.

Egbert, G. G., & Erofeeva, S. Y. (2002). Efficient inverse modeling of barotropic ocean tides. *Journal of Atmospheric and Oceanic Technology*, *19*, 183-204.

Elipot, S., Lumpkin, R., Perez, R. C., Lilly, J. M., Early, J. J., & Sykulski, A. M. (2016). A global surface drifter data set at hourly resolution. *Journal of Geophysical Research: Oceans*, *121*(5), 2937-2966. doi: 10.1002/2016JC011716

Flexas, M. M., Thompson, A. F., Torres, H. S., Klein, P., Farrar, J. T., Zhang, H., & Menemenlis, D. (2019). Global estimates of the energy transfer from the wind to the ocean, with emphasis on near-inertial oscillations. *Journal of Geophysical Research: Oceans*, *124(8)*, 5723-5746. doi: 10.1029/2018JC014453

Fu, L. L., Alsdorf, D., Morrow, R., Rodriguez, E., & Mognard (Eds.), N. (2012). *SWOT: The Surface Water and Ocean Topography Mission: Wide-Swatch Alti-*

This article is protected by copyright. All rights reserved.

Author Manuscript

metric Measurement of Water Elevation on Earth. JPL-Publication (Technical Report).

Gargett, P. J., Hendricks, P. J., Sanford, T. B., Osborn, T. R., & Williams, A. J. (1981). A composite spectrum of vertical shear in the open ocean. *Journal of Physical Oceanography*, *11*, 1258-1271.

Garrett, C., & Munk, W. (1972). Space-Time Scales of Internal Waves. *Geophysical Fluid Dynamics*, *2*, 225-264.

Garrett, C., & Munk, W. (1975). Space-Time Scales of Internal Waves: A progress Report. *Journal of Geophysical Research*, *80 (3)*, 291-297.

Gregg, M. C., Winkel, D. P., & Sanford, T. B. (1993). Varieties of fully resolved spectra of vertical shear. *Journal of Physical Oceanography*, *23*, 124-141.

Halliwell, G. R. (2004). Evaluation of vertical coordinate and vertical mixing algorithms in the HYbrid-Coordinate Ocean Model (HYCOM). *Ocean Modelling*, *7*, 285-322.

Hendershott, M. C. (1972). The effects of solid earth deformation on global ocean tides. *Geophysical Journal of the Royal Astronomical Society*, *29*, 389-402.

Hogan, T. F., Liu, M., Ridout, J. A., Peng, M. S., Whitcomb, T. R., Ruston, B. C., ... Chang, S. W. (2014). The Navy Global Environmental Model. *Oceanography*, *27(3)*, 116-125. Retrieved from `http://dx.doi.org/10.5670/oceanog.2014.73`

Holloway, G. (1983). A conjecture relating oceanic internal waves and small-scale processes. *Atmosphere-Ocean*, *21(1)*, 107-122. doi: 10.1080/07055900.1983.9649159

Jayne, S. R., & St Laurent, L. C. (2001). Parameterizing tidal dissipation over rough topography. *Geophysical Research Letters*, *28*, 811-814.

Kunze, E. (1993). Submesoscale Dynamics near a Seamount. Part II: The Partition of Energy between Internal Waves and Geostrophy. *Journal of Physical Oceanography*, *23*, 2589-2601.

Kunze, E. (2017a). The internal-wave-driven meridional overturning circulation. *Journal of Physical Oceanography*, *47 (11)*, 2673-2689. doi: 10.1175/JPO-D-16-0142.1

Kunze, E. (2017b). Internal-wave-driven mixing: Global geography and budgets. *Journal of Physical Oceanography*, *47 (6)*, 1325-1345. doi: 10.1175/JPO-D-16-0141.1

Kunze, E., Lien, R.-C., Whalen, C. B., Girton, J. B., Ma, B., & Buijsman, M. C. (2023). Seasonal variability of near-inertial/semidiurnal fluctuations and turbulence in the subarctic North Atlantic. *Journal of Physical Oceanography*, *53*, 2717-2735. doi: 10.1175/JPO-D-22-0231.1

Kunze, E., & Sanford, B. (1993). Submesoscale Dynamics near a Seamount. Part I: Measurements of Ertel Vorticity. *Journal of Physical Oceanography*, *23(12)*, 2567-2587.

Kunze, E., & Sanford, T. B. (1984). Observations of near-inertial waves in a front. *Journal of Physical Oceanography*, *14(3)*, 566-581.

Large, W. G., McWilliams, J. C., & Doney, S. C. (1994). Oceanic vertical mixing: a review and a model with a nonlocal boundary layer parameterization. *Reviews of Geophysics*, *32*, 363-403.

Large, W. G., & Yeager, S. G. (2004). *Diurnal and decadal global forcing for ocean and sea-ice models: The data sets and climatologies.* NCAR Tech. Note. Boulder, CO. (TN–460+ST (May)) doi: 10.5065/D6KK98Q6

Leaman, K. D. (1976). Observations on the vertical polarization and energy flux of near-inertial waves. *Journal of Geophysical Research*, *6*, 894-908.

Leaman, K. D., & Sanford, T. B. (1975). Vertical energy propagation of inertial waves: A vector spectral analysis of velocity profiles. *Journal of Geophysical Research*, *80*, 1975-1978.

This article is protected by copyright. All rights reserved.

Author Manuscript

Levine, M. D. (2002). A modification of the garrett-munk internal wave spectrum. *Journal of Physical Oceanography*, *32*, 3166-3181.

Lien, R.-C., & Sanford, B. (2019). Small-Scale Potential Vorticity in the Upper-Ocean Thermocline. *Journal of Physical Oceanography*, *49(7)*, 1845-1872. doi: 10.1175/JPO-D-18-0052.1

Losch, M., Menemenlis, D., Campin, J.-M., Heimbach, P., & Hill, C. N. (2010). On the formulation of sea-ice models. Part 1: effects of different solver implementations and parameterizations. *Ocean Modelling*, *33*, 129–144. doi: 10.1016/j.ocemod.2009.12.008

Luecke, C. A., Arbic, B. K., Richman, J. G., Shriver, J. F., Alford, M. H., Ansong, J. K., ... Zamudio, L. (2020). Statistical Comparisons of temperature variance and kinetic energy in global ocean models and observations: Results from mesoscale to internal wave frequencies. *Journal of Geophysical Research: Oceans*, *125 (5)*. doi: 10.1029/2019JC015306

MacKinnon, J. A., Alford, M. H., Sun, O., Pinkel, R., Zhao, Z., & Klymak, J. (2013a). The latitudinal dependence of shear and mixing in the Pacific transiting the critical latitude for PSI. *Journal of Physical Oceanography*, *43*, 3-16. doi: 10.1175/JPO-D-11-0107.1

MacKinnon, J. A., Alford, M. H., Sun, O., Pinkel, R., Zhao, Z., & Klymak, J. (2013b). Parametric subharmonic instability of the internal tide at 29N. *Journal of Physical Oceanography*, *43*, 17-28. doi: 10.1175/JPO-D-11-0108.1

MacKinnon, J. A., Zhao, Z., Whalen, C. B., Waterhouse, A. F., Trossman, D. S., Sun, O. M., ... Alford, M. H. (2017). Climate Process Team on internal-wave driven ocean mixing. *Bulletin of the American Meteorological Society*, 2429-2454. doi: 10.1175/BAMS-D-16-0030.1

Marshall, J., Hill, C., Perelman, L., & Adcroft, A. (1997). Hydrostatic, quasi-hydrostatic, and nonhydrostatic ocean modeling. *Journal of Geophysical Research: Oceans*, *102 (C3)*, 5733–5752.

Martini, K. I., Alford, M. H., Kunze, E., Kelly, S. M., & Nash, J. D. (2011). Observations of internal tides on the Oregon continental slope. *Journal of Physical Oceanography*, *41*, 1772-1794.

Martini, K. I., Alford, M. H., Kunze, E., Kelly, S. M., & Nash, J. D. (2013). Internal bores and breaking internal tides on the Oregon continental slope. *J. Phys. Oceanogr.*, *43*(1), 120–141.

McComas, C. (1977). Equilibrium mechanisms within the oceanic internal wave field. *Journal of Physical Oceanography*, *7*(6), 836–845.

McComas, C. H., & Bretherton, F. P. (1977). Resonant interactions of oceanic internal waves. *Journal of Geophysical Research*, *82*, 1397–1412. doi: 10.1029/JC082i009p01397

McComas, C. H., & Müller, P. (1981a). The dynamic balance of internal waves. *Journal of Physical Oceanography*, *11*, 970–986.

McComas, C. H., & Müller, P. (1981b). Time scales of resonant interactions among oceanic internal waves. *Journal of Physical Oceanography*, *11*, 139–147.

Menemenlis, D., Campin, J. M., Heimbach, P., Hill, C. N., Lee, T., Nguyen, A. T., ... Zhang, H. (2008). ECCO2: High resolution global ocean and sea ice data synthesis. *Mercator Ocean Quarterly Newsletter*, 13-21.

Metzger, E. J., Smedstad, O. M., Thoppil, P. G., Hurlburt, H. E., Cummings, J. A., Wallcraft, A. J., ... DeHaan, C. J. (2014). US Navy operational global ocean and arctic ice predcition system. *Oceanography*, *27 (3)*, 32-43.

Mitchum, G. T., & Chiswell, S. M. (2000). Coherence of internal tide modulations along the hawaiian ridge. *Journal of Geophysical Research*, *105 (C12)*, 28653-28661.

Morrow, R., Fu, L.-L., Ardhuin, F., Benkiran, M., Chapron, B., Cosme, E., ... Zaron, E. D. (2019). Global observations of finescale ocean surface topography with the surface water and ocean topography (swot) mission. *Frontiers in*

This article is protected by copyright. All rights reserved.

Author Manuscript

Marine Science, *6:232*. doi: 10.3389/fmars.2019.00232

Müller, M., Arbic, B. K., Richman, J. G., Shriver, J. F., Kunze, E. L., Scott, R. B., ... Zamudio, L. (2015). Toward an internal gravity wave spectrum in global ocean models. *Geophysical Research Letters*, *42*, 3474-3481. doi: 10.1002/2015GL063365

Müller, M., Cherniawsky, J. Y., Foreman, M. G. G., & Storch von, J. S. (2012). Global M_2 internal tide and its seasonal variability from high resolution ocean circulation and tide modeling. *Geophysical Research Letters*, *39, L19607*. doi: 10.1029/2012GL053320

Müller, P., Holloway, G., Henyey, F., & Pomphrey, N. (1986). Nonlinear interactions among internal gravity waves. *Reviews of Geophysics*, *24(3)*, 493-536.

Müller, P., Lien, R.-C., & Williams, R. (1988). Estimates of potential vorticity at small scales in the ocean. *Journal of Physical Oceanography*, *18*, 401-416.

Munk, W. (1981). Internal waves and small-scale processes. In *Evolution of physical oceanography: Scientific surveys in honor of henry stommel* (ed. B.A. Warren & C. Wunsch) (p. 264-291). Cambridge Univ. Press, U.K.

Munk, W., & Wunsch, C. (1998). Abyssal recipes ii: energetics of tidal and wind mixing. *Deep-Sea Research I*, *45*, 1977-2010.

Nash, J. D., Alford, M. H., Kunze, E., Martini, K. I., & Kelly, S. (2007). Hotspots of deep ocean mixing on the Oregon continental slope. *Geophys. Res. Lett.*, *34*(L01605), doi:10.1029/2006GL028170.

Nelson, A. D., Arbic, B. K., Menemenlis, D., Peltier, W. R., Alford, M. H., Grisourard, N., & Klymak, J. M. (2020). Improved internal gravity wave spectral continuum in a regional ocean model. *Journal of Geophysical Research Oceans (In-press)*.

Ngodock, H. E., Souopgui, I., Wallcraft, A. J., Richman, J. G., Shriver, J. F., & Arbic, B. K. (2016). On improving the accuracy of the M_2 barotropic tides embedded in a high-resolution global ocean circulation model. *Ocean Modelling*, *97*, 16-26. doi: 10.1016/j.ocemod.2015.10.011

Olbers, D. J. (1976). Nonlinear energy transfer and the energy balance of the internal wave field in the deep ocean. *Journal of Fluid Dynamics*, *74*, 375-399. doi: https://doi.org/10.1017/S0022112076001857

OSiRIS. (2024). *Non-assim HYCOM 1/25° SSH and Surface velocities for 2014* [Dataset]. Retrieved from `https://app.globus.org/file-manager?origin_id=e658b2aa-c5b5-455c-8bd9-49d361ac0bda&origin_path=%2F`

Pinkel, R. (1985). A wavenumber-frequency spectrum of upper ocean shear. *Journal of Physical Oceanography*, *15(11)*, 1453-1469.

Polzin, K. (2004). Heuristic description of internal wave dynamics. *Journal of Physical Oceanography*, *34*, 214–230.

Ponte, R. M., Chaudhuri, A. H., & Vinogradov, V. (2015). Long-period tides in an atmospherically driven, stratified ocean. *Journal of Physical Oceanography*, *45*, 1917-1928. doi: 10.1175/JPO-D-15-0006.1

Ponte, R. M., & Vinogradov, S. V. (2007). Effects of stratification on the large-scale ocean response to barometric pressure. *Journal of Physical Oceanography*, *37*, 245-258. doi: doi:10.1175/JPO3010.1

Qiu, B., Chen, S., Klein, P., Wang, J., Torres, H., Fu, L.-L., & Menemenlis, D. (2018). Seasonality in transition scale from balanced to unbalanced motion in the world ocean. *Journal of Physical Oceanography*. doi: 10.1175/JPO-D-17-0169.1

Qiu, B., Nakano, T., Chen, S., & Klein, P. (2017). Submesoscale transition from geostrophic flows to internal waves in the northwestern Pacific upper ocean. *Nature Communations*. doi: 10.1038/ncomms14055

Raja, K. J., Buijsman, M. C., Shriver, J. F., Arbic, B. K., & Siyanbola, O. (2022). Near-inertial wave energetics modulated by background flows in a global model simulation. *Journal of Physical Oceanography*, *52*, 823-840. doi:

This article is protected by copyright. All rights reserved.

Author Manuscript

https://doi.org/10.1175/JPO-D-21-0130.1

Ray, R. D. (1998). Ocean self-attraction and loading in mumerical tidal models. *Marine Geodesy*, *21*, 181-192.

Ray, R. D., & Mitchum, G. T. (1996). Surface manifestation of internal tides generated near Hawaii. *Geophysical Research Letters*, *23*, 2101-2104.

Richman, J. G., Arbic, B. K., Shriver, J. F., Metzger, E. J., & Wallcraft, A. J. (2012). Inferring dynamics from the wavenumber spectra of an eddying global ocean model with embedded tides. *Journal of Geophysical Research*, *117, C12012*. doi: 10.1029/2012JC008364

Rocha, C. B., Chereskin, T. K., Gille, S. T., & Menemenlis, D. (2016a). Mesoscale to submesoscale wavenumber spectra in Drake Passage. *Journal of Physical Oceanogarphy*, *46*, 601-620. doi: 10.1175/JPO-D-15-0087.1

Rocha, C. B., Chereskin, T. K., Gille, S. T., & Menemenlis, D. (2016b). Seasonality of submesoscale dynamics in the Kuroshio Extension. *Journal of Geophysical Research*, *43 (21)*, 11304-11311. doi: 10.1002/2016GL071349

Savage, A. C., & Arbic, B. K. (2017). *Dataset of spectral decomposition of internal gravity waves sea surface height in global models [Dataset].* Github. `https://github.com/annasavage/McLane_profiler_data`.

Savage, A. C., Arbic, B. K., Alford, M. H., Ansong, J. K., Farrar, J. T., Menemenlis, D., ... Zamudio, L. (2017). Spectral decomposition of internal gravity waves sea surface height in global models. *Journal of Geophysical Research: Oceans*, *122*. doi: 10.1002/2017JC013009

Savage, A. C., Arbic, B. K., Richman, J. G., Shriver, J. F., Alford, M. H., Buijsman, M. C., ... Zamudio, L. (2017). Frequency content of sea surface height variability from internal gravity waves to mesoscale eddies. *Journal of Geophysical Research*, *122 (3)*. doi: 10.1002/2016JC012331

Shriver, J. F., Arbic, B. K., Richman, J. G., Ray, R. D., Metzger, E. J., Wallcraft, A. J., & Timko, P. G. (2012). An evaluation of the barotropic and internal tides in a high resolution global ocean circulation model. *Journal of Geophysical Research*, *117, C10024*. doi: 10.1029/2012JC008170

Simmons, H. L., & Alford, M. H. (2012). Simulating the long-range swell of internal waves generated by ocean storms. *Oceanography*, *25 (2)*, 30-41.

Simmons, H. L., Hallberg, R. W., & Arbic, B. K. (2004). Internal wave generation in a global baroclinic tide model. *Deep-Sea Research II*, *51*, 3043-3068.

Skitka, J., Arbic, B. K., Thakur, R., Menemenlis, D., Peltier, W. R., Pan, Y., ... Ma, Y. (2024). Probing the nonlinear interactions of supertidal internal waves using a high-resolution regional ocean model. *Journal of Physical Oceanography*, *54*, 399–425. doi: https://doi.org/10.1175/JPO-D-22-0236.1

Solano, M. S., Buijsman, M. C., Shriver, J. F., Magalhaes, J., da Silva, J., Jackson, C., ... Barkan, R. (2023). Nonlinear internal tides in a realistically forced global ocean simulation. *Journal of Geophysical Research Oceans*, *128*, e2023JC019913. doi: https://doi.org/10.1029/2023JC019913

Stammer, D., Ray, R. D., Andersen, O. B., Arbic, B. K., Bosch, W., Carrere, L., ... Yi, Y. (2014). Accuracy assessment of global barotropic ocean tide models. *Reviews of Geophysics*, *52*. doi: 10.1002/2014RG000450

Sugiyama, Y., Niwa, Y., & Hibiya, T. (2009). Numerically reproduced internal wave spectra in the deep ocean. *Journal of Geophysical Research*, *36 (L07601)*. doi: 10.1029/2008GL036825

Thakur, R., Arbic, B. K., Menemenlis, D., Momeni, K., Pan, Y., Peltier, W. R., ... Ma, Y. (2022). Impact of vertical mixing parameterizations on internal gravity wave spectra in regional ocean models. *Geophysical Research Letters*, *49*, e2022GL099614. doi: 10.1029/2022GL099614

Torres, H. S., Klein, P., Menemenlis, D., Qiu, B., Su, Z., Wang, J., ... Fu, L.-L. (2018). Partitioning ocean motions into balanced motions and internal gravity waves: A modelling study in anticipation of future space missions. *Journal of*

This article is protected by copyright. All rights reserved.

Author Manuscript

Geophysical Research Oceans, *123*, 8084-8015. doi: 10.1029/2018JC014438

Wang, C., Liu, Z., & Lin, H. (2023). A simple approach for disentangling vortical and wavy motions of oceanic flows. *Journal of Physical Oceanography*, *53*, 1237-1249. doi: 10.1175/JPO-D-22-0148.1

Wang, J., Fu, L.-L., Qiu, B., Menemenlis, D., Farrar, J. T., Chao, Y., ... Flexas, M. (2018). An observing system simulation experiment for the calibration and validation of the surface water ocean topography sea surface height measurement using in situ platforms. *Journal of Atmospheric and Oceanic Technology*, *35*, 281–297. doi: https://doi.org/10.1175/JTECH-D-17-0076.1

Wang, J., Fu, L.-L., Torres, H. S., Chen, S., Qiu, B., & Menemenlis, D. (2019). On the spatial scales to be resolved by the surface water and ocean topography ka-band radar interferometer. *Journal of Atmospheric and Oceanic Technology*, *36*, 87-99. doi: 10.1175/JTECH-D-18-0119.1.

Waterhouse, A. F., Hennon, T., Kunze, E., MacKinnon, J. A., Alford, M., Pinkel, R., ... Hummon, J. M. (2022). Global Observations of Rotary-with-Depth Shear Spectra. *Journal of Physical Oceanography*, *52*, 3241-3258. doi: 10.1175/JPO-D-22-0015.1

Wright, D. G., Pawlowicz, R., McDougall, T. J., Feistel, R., & Marion, G. M. (2011). Absolute Salinity, "Density Salinity" and the Reference-Composition Salinity Scale: present and future use in the seawater standard TEOS-10. *Ocean Science*, *7*, 1-26. doi: 10.5194/os-7-1-2011

Wunsch, C. (2016). Rough notes on internal waves in the ECCO2 1/48° global estimate with acoustic implications. *Unpublished Manuscript*.

Wunsch, C., & Ferrari, R. (2004). Vertical mixing, energy and the general circulation of the ocean. *Annual Review of Fluid Mechanics*, *36*, 281-314.

Yu, X., Ponte, A. L., Elipot, S., Menemenlis, D., Zaron, E. D., & Abernathey, R. (2019). Surface kinetic energy distributions in the global oceans from a high-resolution numerical model and surface drifter observations. *Geophysical Research Letters*, *46*(16), 9757–9766. doi: 10.1029/2019GL083074

Zhao, Z., Alford, M. H., MacKinnon, J. A., & Pinkel, R. (2010). Long-range propagation of the semi-diurnal internal tide from the Hawaiian ridge. *Journal of Physical Oceanography*, *40*, 713-736.

This article is protected by copyright. All rights reserved.